Figure 1: Overview of study area in the Ukrainian Carpathians, showing main tectonic nappes and sample locations. A) Inset shows setting of the Carpathian belt in Europe and location of the study region. B) Tectonic units are highlighted in different colours and follow Schmid et al. (2008), with reinterpreted names to be closer to the regional designation of the lithostratigraphy. Marmarosh and Magura nappes are both represented in green. Thin lines represent major intra-nappe faults. Grey thick line marks the location of the cross section. C) Simplified tectonic cross section (after Nakapelyukh et al., 2018); EEUM: East European Margin. Major faults delimiting the nappes are in bold red lines, thin red lines indicate intra-nappe faults. Sample locations are projected onto the section.

785
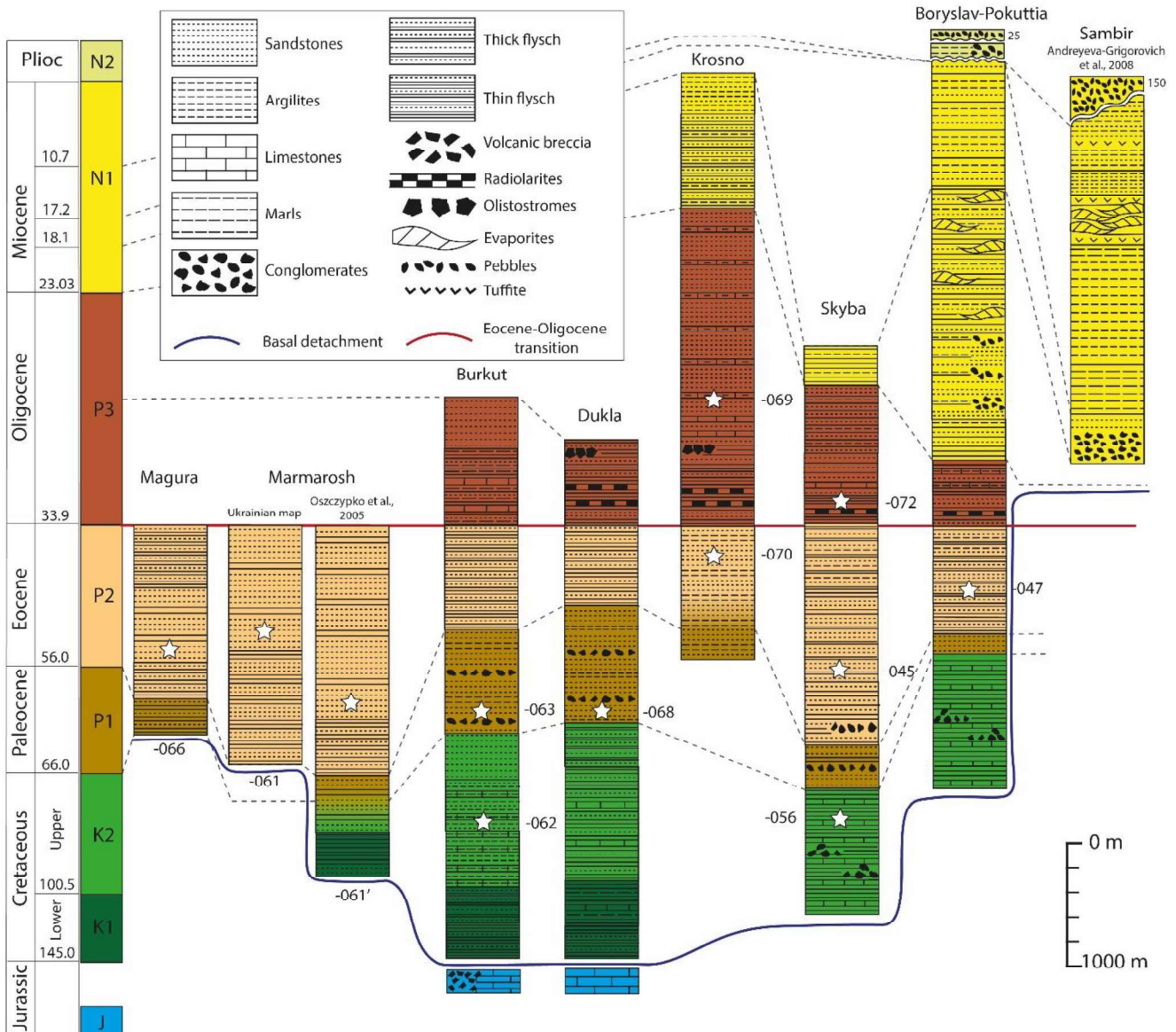
Figure 2: Regional stratigraphy of the Ukrainian Carpathian nappes, mainly from Ukrainian geological maps (Docin, 1963; Vachtchenko et al., 2003; Gerasimov et al., 2005; Matskiv et al., 2008, 2009). Stars mark the sample locations in the nappe stratigraphy; samples are identified by their suffix. Dark blue line marks the décollement horizon of the nappes. Jurassic rocks are integrated in the Burkut and Dukla nappes. Two stratigraphies are indicated for the Marmarosh nappe, one from the Ukrainian geological map, the other from Oszczypko et al. (2005). The Sambir nappe stratigraphy is after Andreyeva-Grigorovich et al. (2008) with adaptation to the new stratigraphic limits of Parathethys stages(Krijgsman and Piller, 2012). The stratigraphic columns depicted here are the closest ones available to the sampling site of each sample. The lateral variations in thickness or nature of deposition within individual nappes are not represented by these logs.

790

795
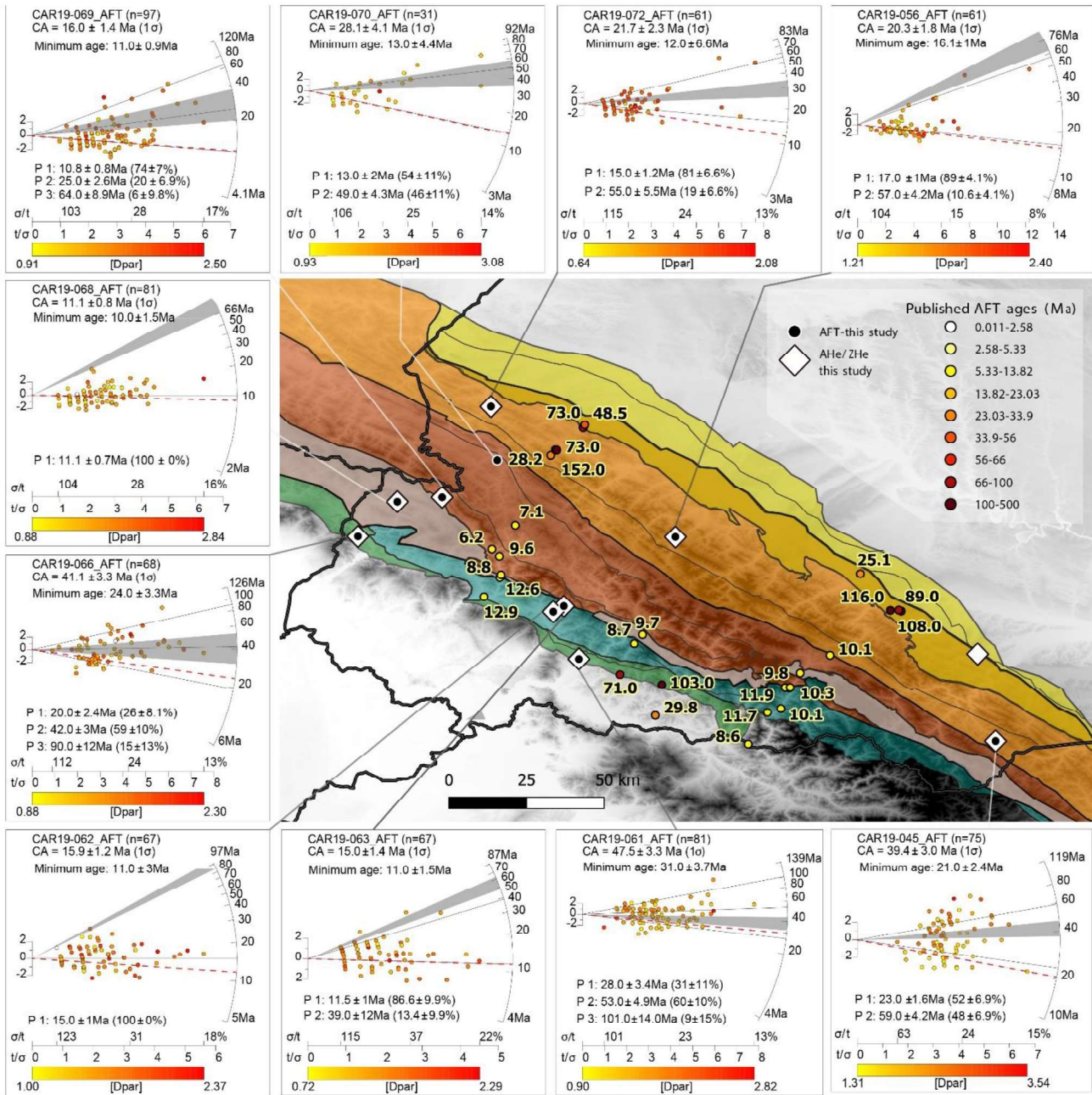
Figure 3: AFT data from this study shown as radial plots (centred on the central age, which is reported below the sample code as CA); individual single-grain ages in radial plots are coloured according to Dpar value. Grey band in radial plots indicates depositional age, dashed lines are different age populations (P1, P2, etc.); red dashed line is minimum age. Coloured circles on map show AFT central ages from previous studies (Nakapelyukh et al., 2017, 2018; Andreucci et al., 2013, 2015). Base map shows different nappes, with colour scheme as in Figure 1.

800
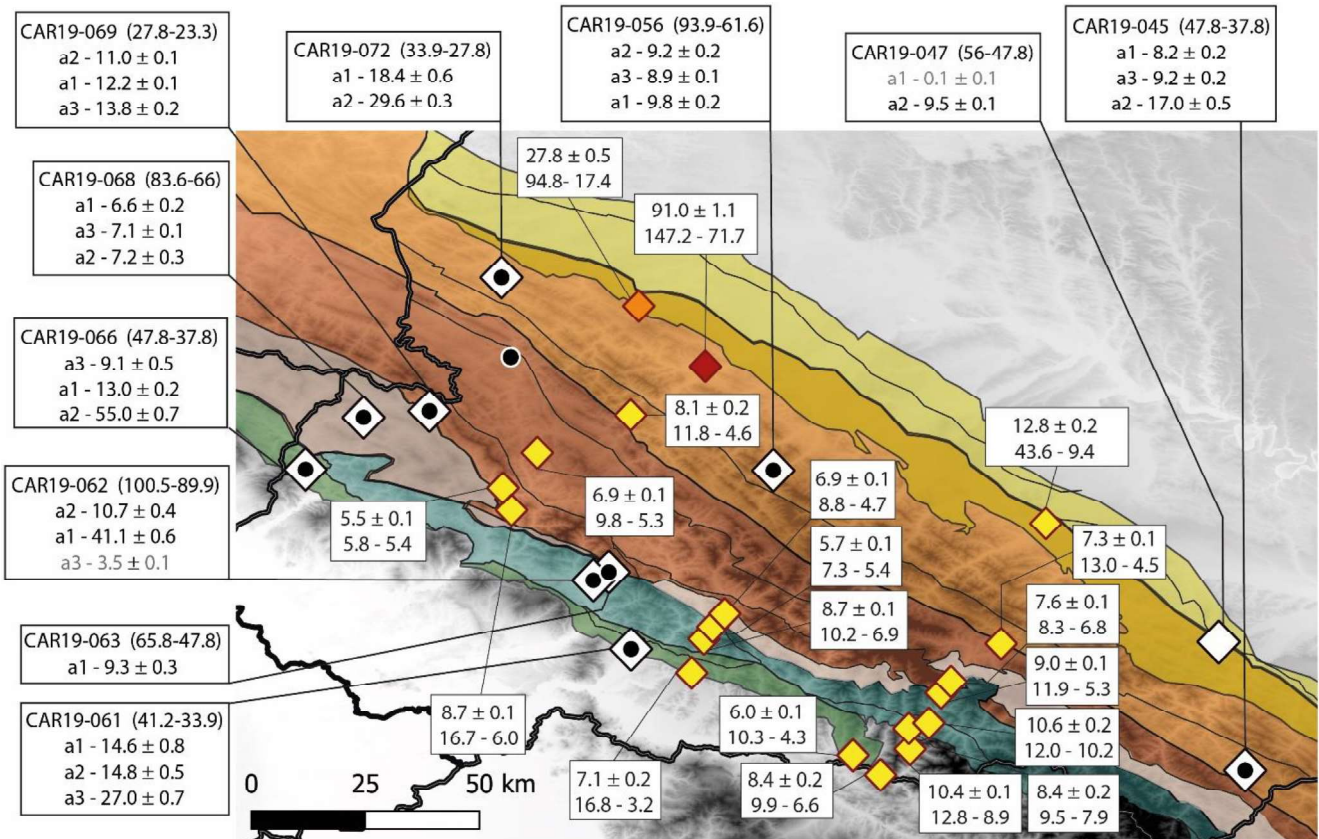
Figure 4: Apatite (U-Th)/He ages in the Ukrainian Carpathians. Symbols and colour scale for the data are as indicated in Figure 3. Single-grain ages, corrected for α-ejection, from this study are detailed next to the map frame (numbers in parentheses next to sample code denote the depositional age range). Previously published data (Andreucci et al., 2013, 2015; Merten et al., 2010) are reported on the map as the average age and associated uncertainty, with maximum and minimum single-grain ages below. Ages in grey are interpreted to be outliers and are not used in the models or in our interpretations.
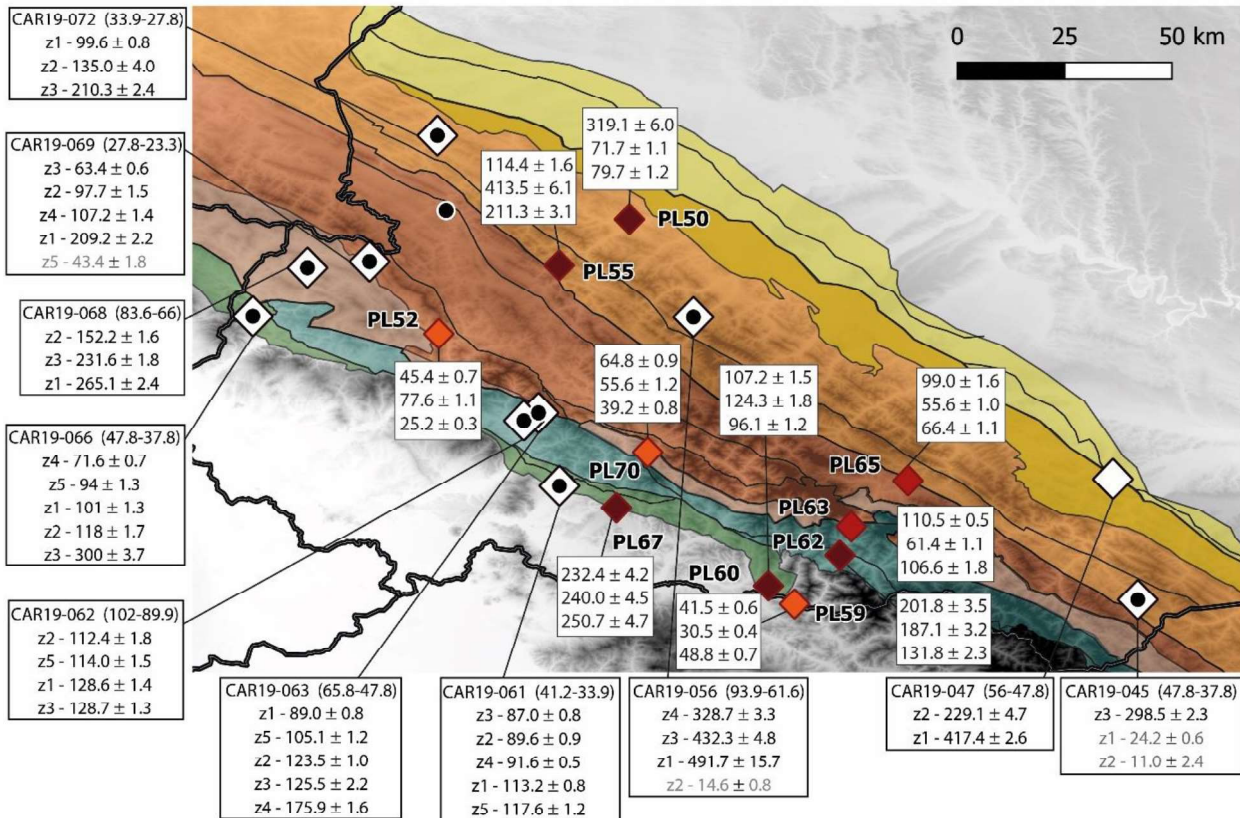
Figure 5: Zircon (U-Th)/He ages in the Ukrainian Carpathians. Symbols and colour scale for the data are as indicated in Figure 3. Single-grain ages, corrected for α-ejection, from this study are detailed next to the map frame (numbers in parentheses next to sample code denote the depositional age range). Previously published data (Andreucci et al., 2015) are reported on the map as the average age and associated uncertainty, with maximum and minimum single-grain ages below. Ages in grey are interpreted to be outliers and are not used in the models or in our interpretations.
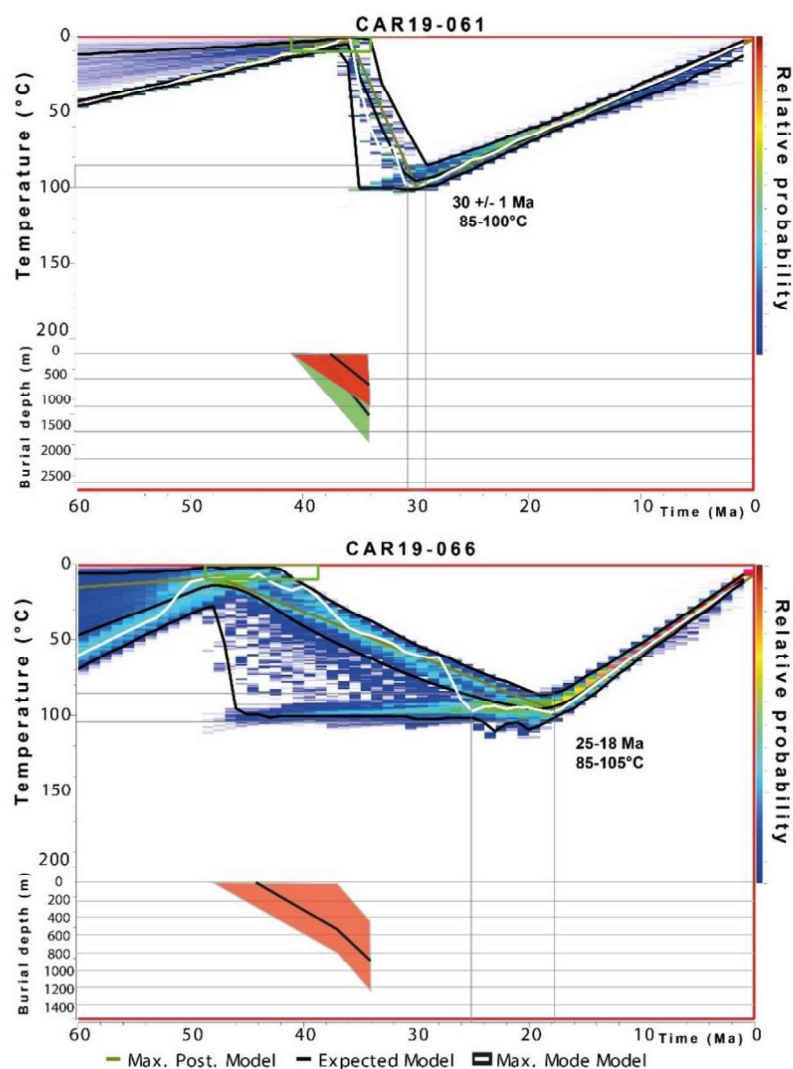
Figure 6: Modelled thermal histories and associated burial diagrams for samples CAR19-061 and -066 from the Marmarosh and Magura nappes, respectively. For sample CAR19-061, burial diagrams are shown both for the stratigraphy from the Ukrainian geological map (orange) and the revised stratigraphy proposed by Oszczypko et al. (2005; green) as shown in Fig. 2. Peak burial temperature and time are highlighted by grey boxes.
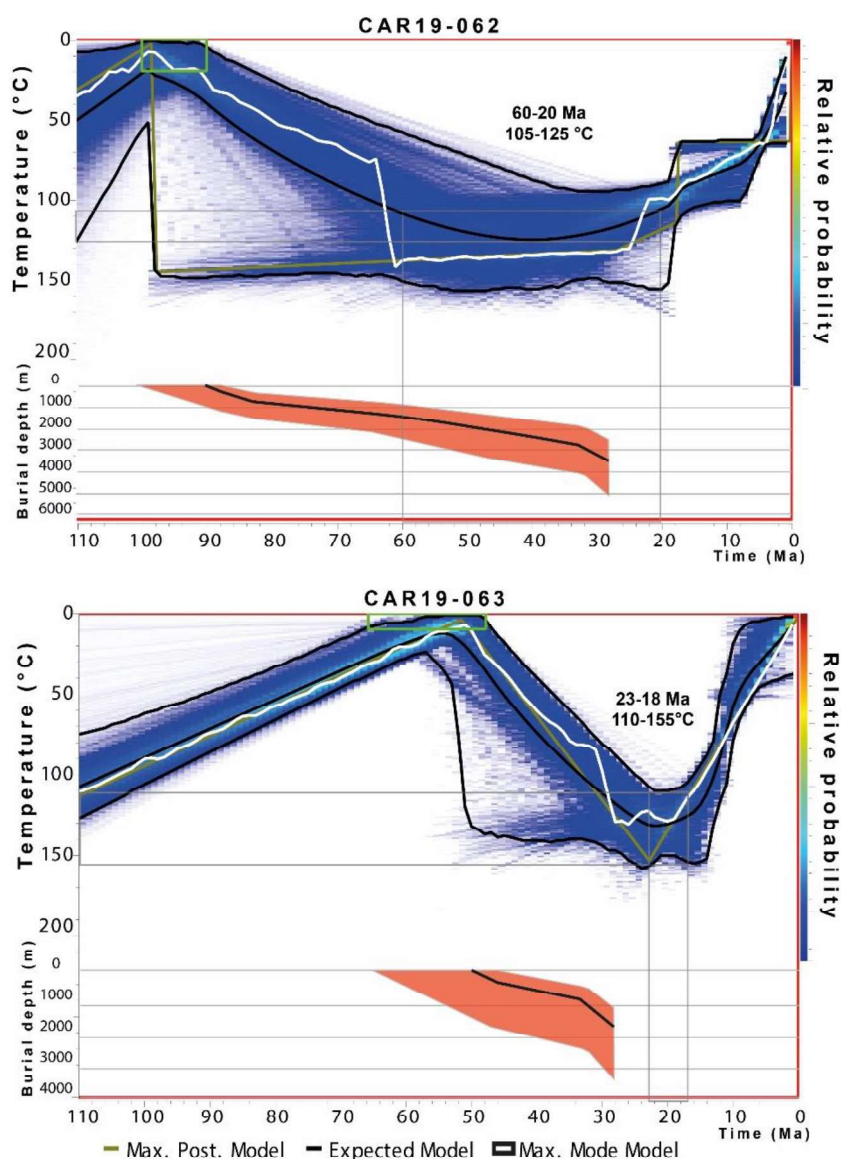
Figure 7: Modelled thermal histories and associated burial diagrams for samples CAR19-062 and 063 from the Burkut nappe. Peak burial temperature and time are highlighted by grey boxes.
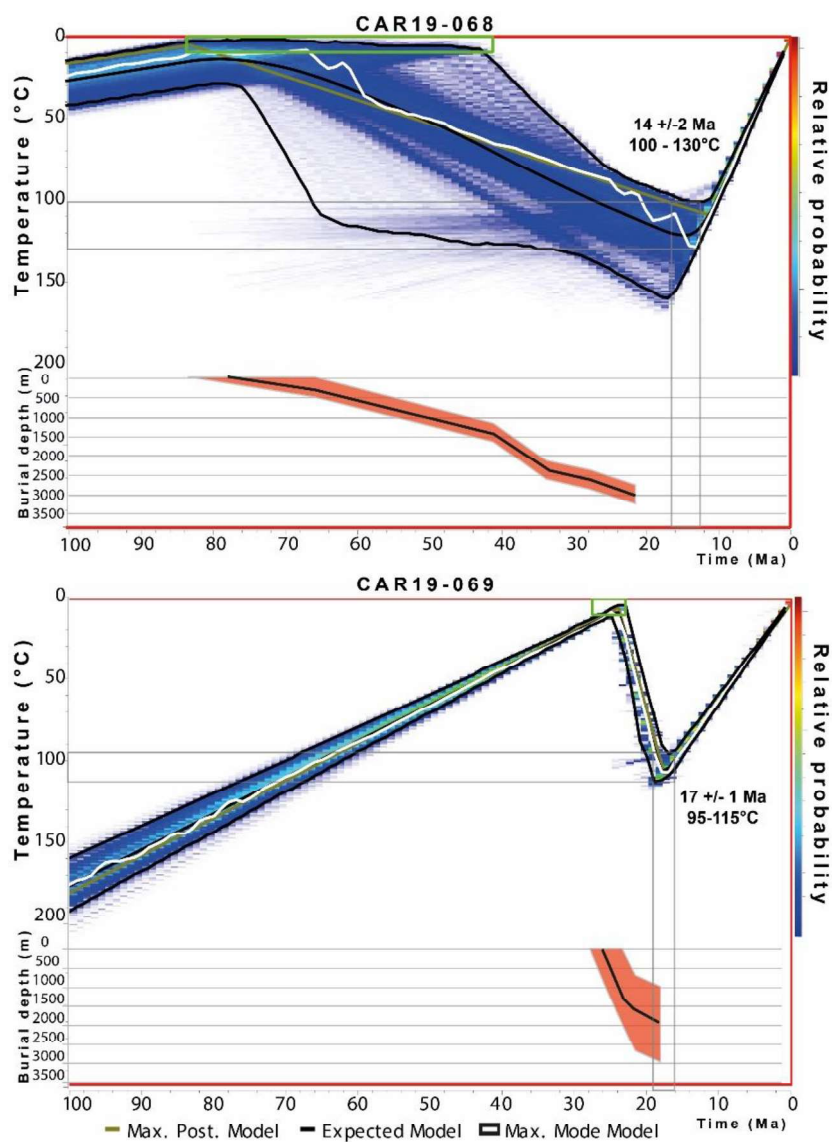
Figure 8: Modelled thermal histories and associated burial diagrams for samples CAR19-068 and 069 from the Dukla and Krosno nappe, respectively, and associated burial diagrams. Peak burial temperature and time are highlighted by grey boxes.
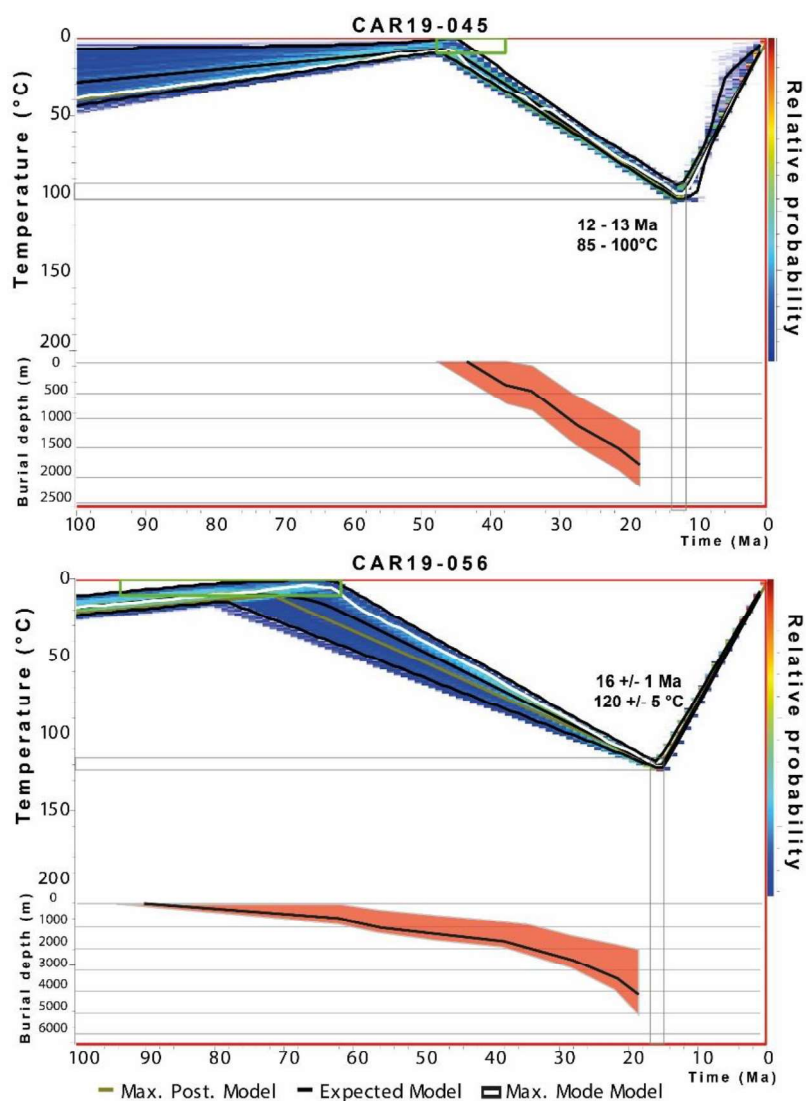
Figure 9: Modelled thermal histories and associated burial diagrams for samples CAR19-045 and -056 from the Skyba nappe and associated burial diagrams. Peak burial temperature and time are highlighted by grey boxes.
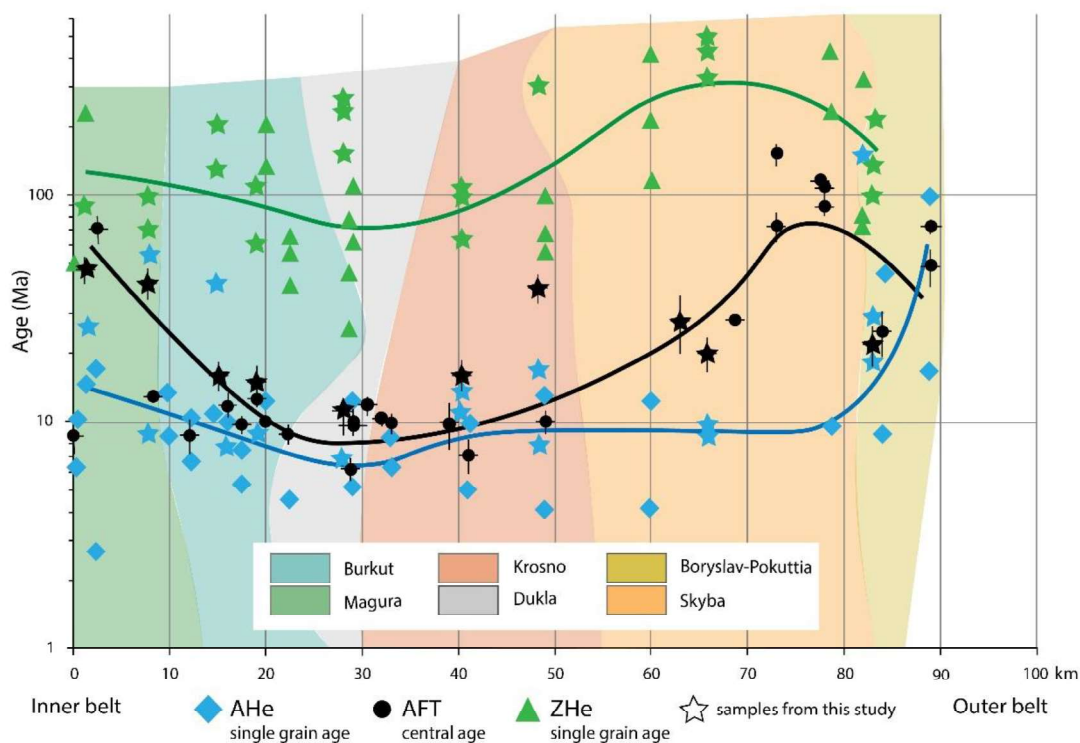
Figure 10: Distribution of thermochronometer ages across the Ukrainian Carpathians as a function of distance, measured from the inner belt to the outer belt. The figure shows a compilation of previously published ages with symbols according to the system; samples from this study ages are shown with stars. Single-grain AHe and ZHe ages are shown; AFT data are represented as central ages together with the 2σ error. Note that the age axis is logarithmic. Curves outline the overall age pattern.
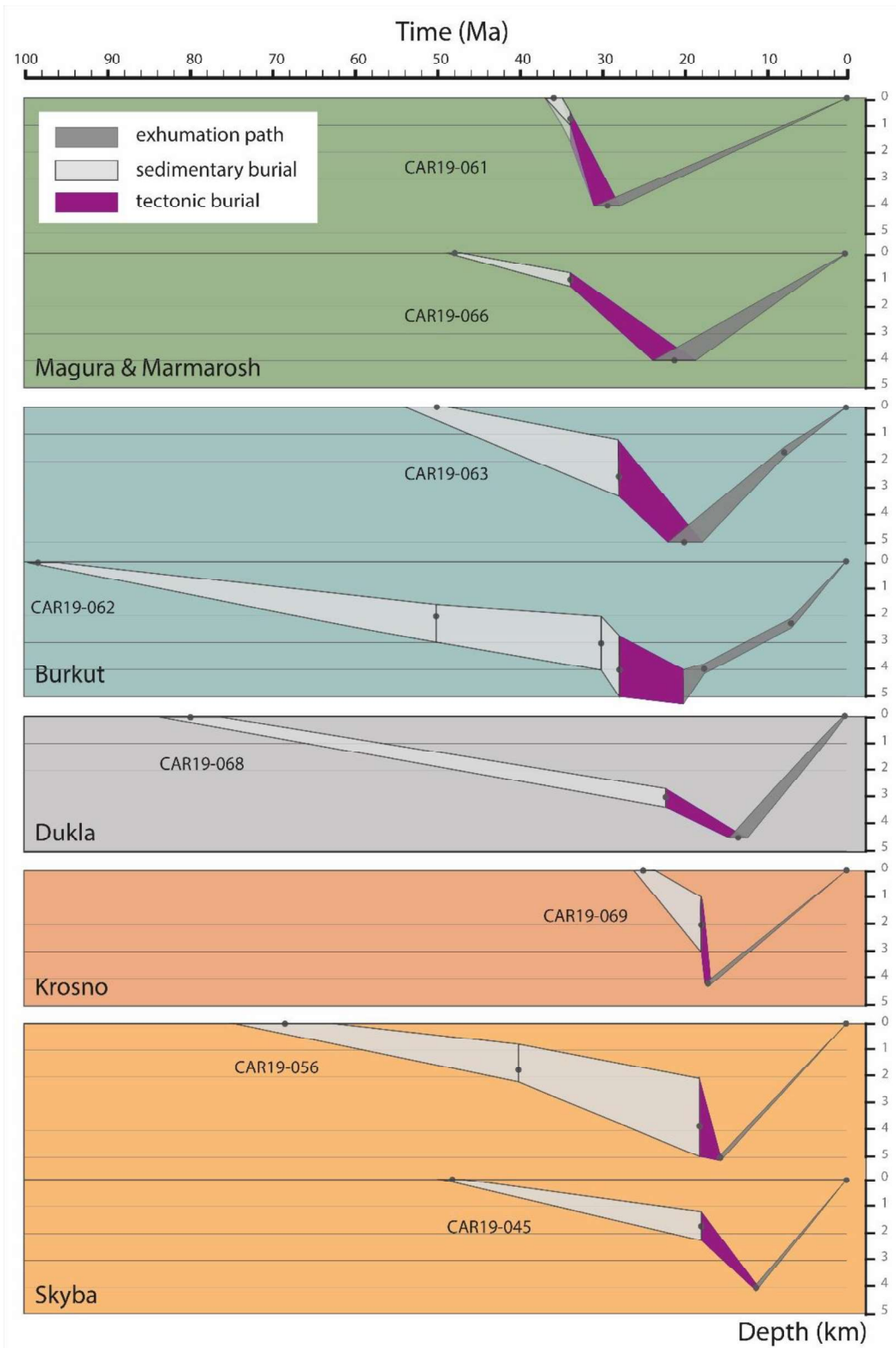
Figure 11: Time-depth evolution of each sample. The depths of the samples through time was estimated from the burial diagrams and the thermal histories modelled in Figs. 7-10, using a geothermal gradient of 25°C/km. Tectonic burial refers to the accretion and burial by thrusting. Time-depth paths are sorted from the innermost (top) to the outermost sample (bottom) of this study. Box colours represent each tectonic nappe as in Figure 1.
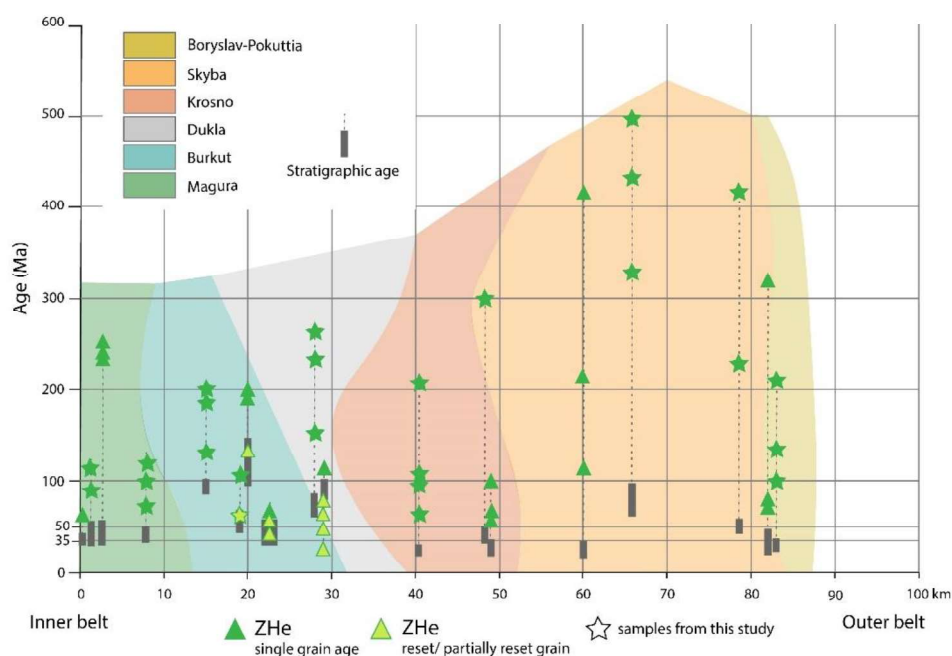
Figure 12: Distribution of ZHe ages across the Ukrainian Carpathians as a function of distance from the inner to the outer belt. Stars represent data from this study; triangles are previously published data. Grey boxes indicate the stratigraphic age of the sample and dashed line mark the corresponding thermochronological ages. Coloured areas represent the different nappes.
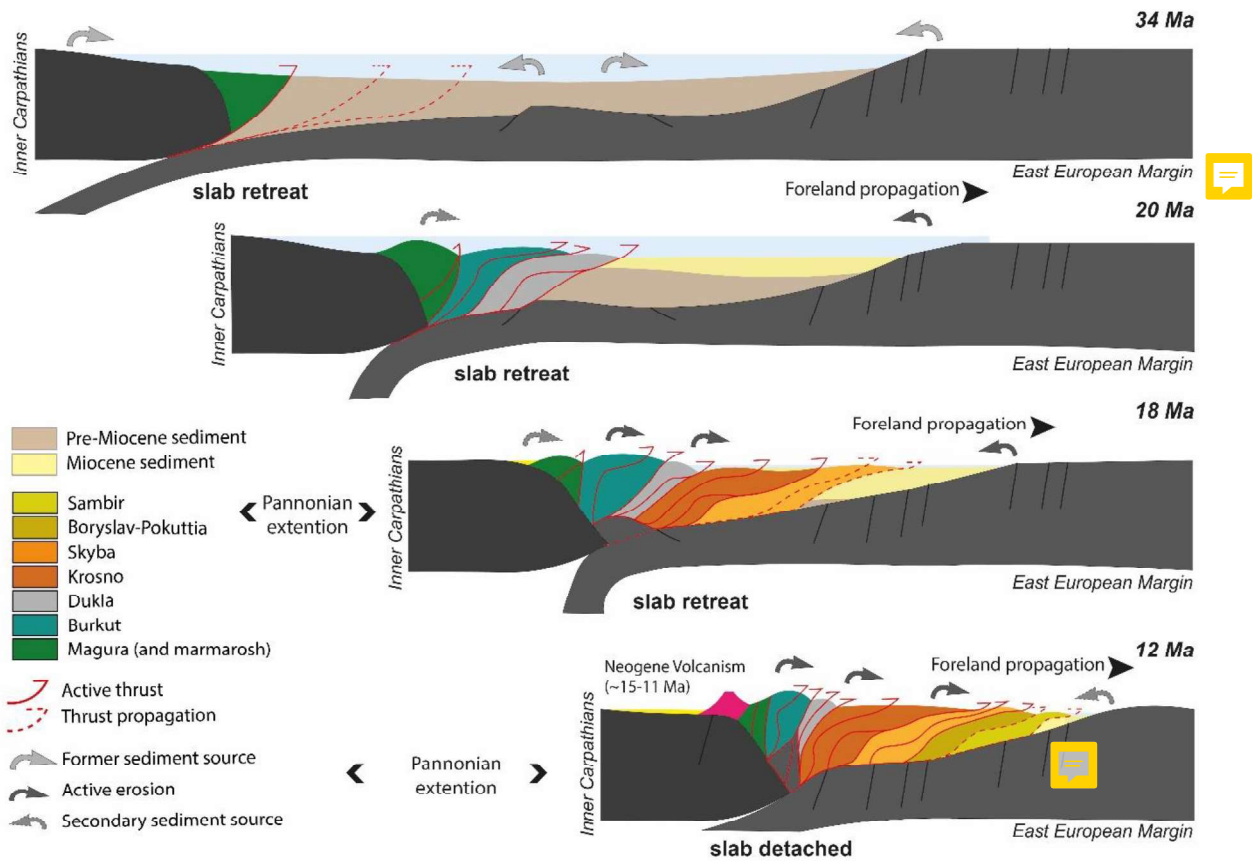
Figure 13: Sketch of the construction of the Ukrainian Carpathian wedge from 34 Ma to 12 Ma. Dashed red line are thrusts that will propagate on the next time step. Full red lines with arrows on top are thrust that are active or will reactivate, full red lines without arrows are sealed. Light grey arrows show source of sediment supply to the different basins. Dark grey arrows are for the active erosion of the nappe. For 12 Ma sketch, foreland propagation terminated around 11.5 Ma (Nemčok et al., 2006), and Neogene volcanism is linked to Pannonian extension (Tiliță et al., 2018) Vertical and horizontal scales are exaggerated.

945
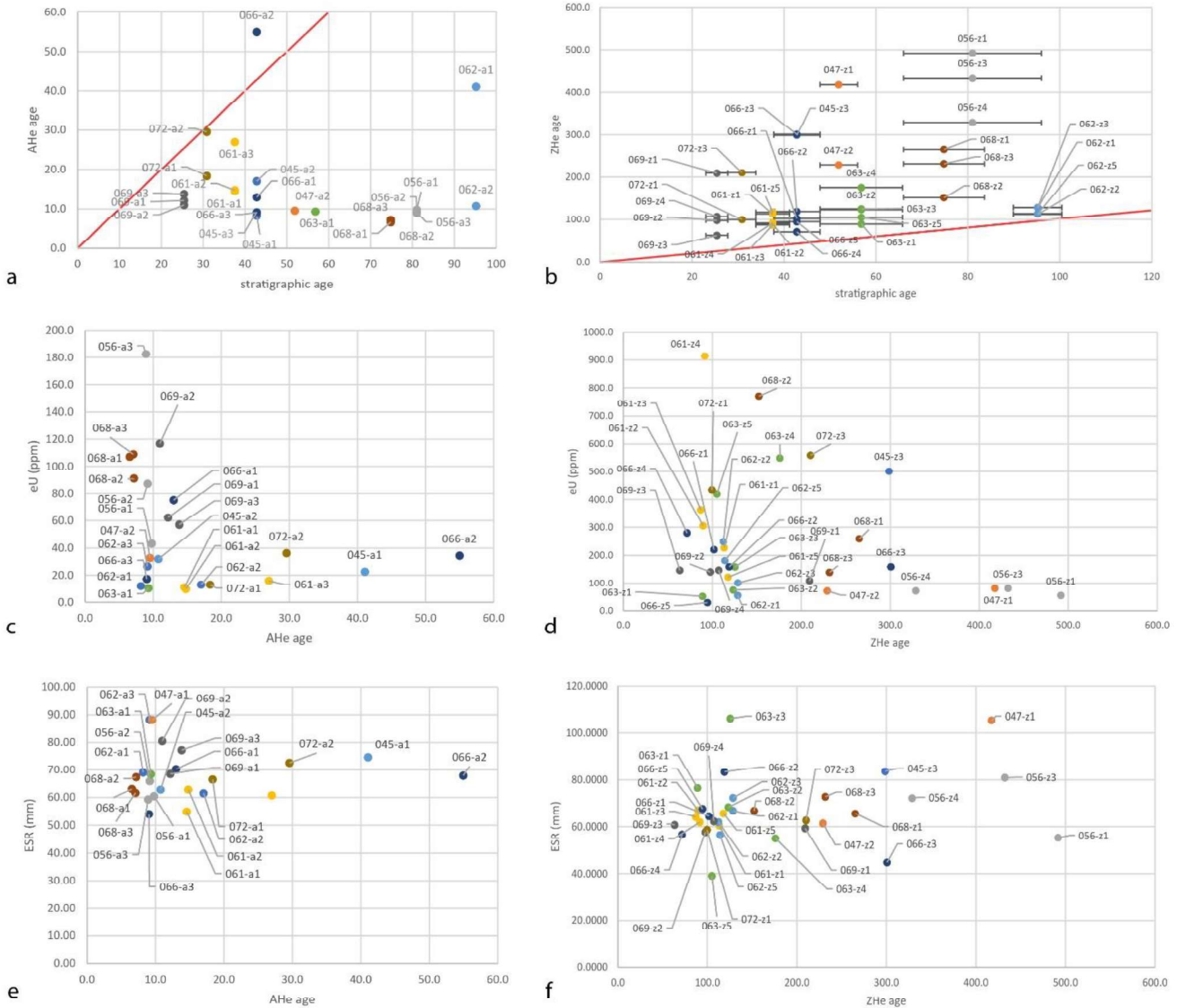
Figure A 1: Circle colour refer to a sample, the same colour code is applied for all graphs. a) Graphic of the AHe single grain age compared to the stratigraphic age. CAR19-066_a2 is the only non-reset grain. b) ZHe single grain age compared to the stratigraphic age. ZHe are non-reset and mark the sediment source age of exhumation. c) AHe single grain age as a function of eU (ppm) content. d) ZHe single grain age as a function of eU (ppm) content. e) AHe single-grain age as a function of ESR (equivalent sphere radius, in mm). f) ZHe single-grain age as a function of ESR.

Construction of the Ukrainian Carpathian Wedge from low-temperature thermochronology and tectono-stratigraphic analysis

Marion Roger[1], Arjan de Leeuw[1], Peter van der Beek[2], Laurent Husson[1], Edward R. Sobel[2], Johannes Glodny[3] and Matthias Bernet[1]

5 [1]Institut des Sciences de la Terre (ISTerre), Université Grenoble Alpes, CNRS, IRD, 38000 Grenoble, France
[2]Institut für Geowissenschaften, Universität Potsdam, 14476 Potsdam, Germany
[3]GFZ German Research Centre for Geosciences, Potsdam 14473, Germany

Correspondence to: Marion Roger (marion.roger@univ-grenoble-alpes.fr)

Abstract. The evolution of orogenic wedges can be determined through stratigraphic and thermochronological analysis. We
10 used apatite fission-track (AFT) and apatite and zircon (U-Th-Sm)/He (AHe and ZHe) low-temperature thermochronology to assess the thermal evolution of the Ukrainian Carpathians, a prime example of an orogenic wedge forming in a retreating subduction zone setting. Whereas most of our AHe ages are reset by burial heating, eight out of ten of our AFT ages are partially reset, and all ZHe ages are non-reset. We inverse-modelled our thermochronology data to determine the time-temperature paths of six out of the 8 nappes composing the wedge. The models were integrated with burial diagrams derived
15 from the stratigraphy of the individual nappes, which allowed us to distinguish sedimentary from tectonic burial. This analysis reveals that accretion of successive nappes and their subsequent exhumation mostly occurred sequentially, with an apparent exhumation rate increase towards the external nappes. Following a phase of tectonic burial, the nappes were generally exhumed when a new nappe was accreted, whereas, in one case, duplexing resulted in prolonged burial. An early orogenic wedge formed with the accretion of the innermost nappe at 34 Ma, leading to an increase in sediment supply to the
20 remnant basin. Most of the other nappes were accreted between 28-18 Ma. Modelled exhumation of the outermost nappe started at 12 Ma, and was accompanied by out-of-sequence thrusting. The latter was linked to emplacement of the wedge onto the European platform and consequent slab detachment. The distribution of thermochronological ages across the wedge, showing non-reset ages in both the inner and outer part of the belt, suggests that the wedge was unable to reach dynamic equilibrium for a period long enough to fully reset all thermochronometers. Non-reset ZHe ages indicate that sediments in
25 the inner part of the Carpathian embayment were mostly supplied by the Inner Carpathians, while sediments in the outer part of the basin were derived mostly from the Trans-European suture zone or the European margin. Our results suggest that during the accretionary phase, few sediments were recycled from the wedge to the foredeep. Most of the sediments exhumed from the Ukrainian Carpathian wedge were likely transported directly to the present pro- and retro- foreland basins.

30 1 Introduction

Fold-and-thrust belts result from the accretion, stacking and exhumation of sediments from pre-existing basins trapped in convergence zones. These basins frequently evolve from rifted passive margins to orogens (e.g., Stockmal et al., 1986) and the stratigraphy of these basins provides a record of convergence-zone dynamics and the onset of orogeny, in particular when the sedimentary record is combined with subsequent exhumation paths that can be retrieved from detrital zircon and

35 apatite grains using low-temperature thermochronology.

Sediments in the antecedent basin are brought to depth by sedimentary burial and integrated into the wedge through nappe stacking processes in two steps. Sediment deposition in the basin may bury earlier deposits under several kilometers of overburden. Sediment accumulation is bound to accelerate as the orogenic belt propagates toward the basin, by a combination of enhanced erosion of the growing wedge and its backstop, and creation of accommodation space by flexure of

40 the underlying plate (Simpson, 2006; Sinclair, 2012). Tectonic nappe stacking may then bury the sediments further when the frontal thrust overrides the pre-existing basin. When the frontal thrust subsequently propagates to the external margin of the newly formed nappe, the nappe becomes incorporated into the wedge and may start to be uplifted and exhumed. The next accreted nappe will follow the same development until plate convergence stops. Overthrusting of a nappe may entrain a phase of internal deformation in the orogenic wedge that causes rock- and surface uplift (Hoth et al., 2007; Sinclair and

45 Naylor, 2012). Steady state in the wedge may potentially be reached if the tectonic influx of material into the wedge and the outflow through erosion balance one another, so that the elevation and width of the wedge remain constant (Willett et al. 1993).

In the Carpathian fold-and-thrust belt, the main driver of foreland-basin subsidence and frontal accretion is slab roll-back rather than plate convergence (e.g., Royden and Faccenna, 2015). The elevation and width of the wedge are insufficient for

50 the weight of the wedge to have created the observed (up to 10 km) deep Carpathian foreland basin (Royden and Karner, 1984; Royden, 1993). Previous studies in the East and Southeast Carpathians of Romania have focused on the timing of nappe-stacking and exhumation of the wedge. Using low-temperature thermochronology on profiles to quantify the erosion pattern on both sides of the wedge, Sanders et al. (1999) concluded that the southeast Carpathians can be treated as a doubly-vergent critical wedge, where the back thrusts are covered by Neogene volcanic rocks and sediments that accumulated in the

55 retro-foreland basin. Further studies, however, inferred that the doubly-vergent wedge concept cannot be directly applied to the east and southeast Carpathians, and that this belt is a singly vergent wedge and evolved through forward propagation of deformation over the subducting plate followed by significant out-of-sequence deformation (Matenco et al., 2010; Merten et al., 2010). In contrast, the western Carpathians might correspond to a doubly vergent wedge as back thrusts are present and some involve basement blocks (Mazzoli et al., 2010; Castelluccio et al., 2016).

60 Convergence in the Carpathians was mostly oblique to the East European Margin (EEM), except in the Ukrainian Carpathians, where it occurred perpendicular to the margin. This makes the Ukrainian Carpathians a promising site to resolve wedge dynamics, as well as the kinematics and drivers of nappe stacking. The structure and timing of nappe

accretion in the Ukrainian Carpathians was previously studied by Nakapelyuk et al. (2018), through balanced cross sections and low-temperature thermochronology. Their study revealed very rapid convergence starting in the Miocene, when most of the nappes were accreted and subsequently exhumed (Fig. 1). Despite the analyses of Nakapelyuk et al. (2018) and the earlier study of Andreucci et al. (2015), the density of thermochronological data in the Ukrainian Carpathians remains low in comparison with the rest of the mountain belt.

To better understand the dynamics of accretionary wedge formation during slab roll-back and to constrain sediment fluxes in this type of orogen, we study the accretion-collision and exhumation phases of the Ukrainian Carpathian wedge from the Oligocene onward using thermal-history modelling based on low-temperature thermochronology and stratigraphic analysis. In particular, we constrain the timing and amount of sedimentary and tectonic burial for each nappe, as well as its subsequent exhumation.

2 Geological context

The Carpathian belt is the result of the collision of the Tisza-Dacia and Alps-Carpathian-Pannonian (ALCAPA) micro-plates with the East European margin (Csontos et al., 1992; Schmid et al., 2008). These two microplates jointly moved to the North from the Late Cretaceous (Santonian; ~84 Ma) to the Oligocene (~34 Ma). From then on, they moved northeast into the Carpathian embayment, a deep-water area of oceanic to thinned continental crust with intervening ridges formed during Tethyan rifting (Handy et al., 2015). Most of the microplates' motion was accommodated by roll-back of the subducting European oceanic crust and rifted continental margin. ALCAPA motion was also promoted by extrusion from the convergence zone of the Alps (Sperner et al., 2002). Nappe accretion into the outer Carpathian thin-skinned wedge started in the Oligocene (M. Sandulescu, 1975; Nemčok et al., 2006; Schmid et al., 2008). The age of the terminal frontal thrust of the Outer Carpathians, which can be used as a proxy for collision, becomes younger from northwest to southeast along the orogen (Nemčok et al., 2006). Oblique collision occurred in the northwest Carpathians from 17-15 Ma (Nemcok et al., 2006 and references therein). Subsequent subduction roll-back towards the east led to continued nappe accretion in front of the wedge, coincident with back-arc extension in the Pannonian Basin (Tari et al., 1992; Horváth and Cloetingh, 1996). This was followed by collision in the Ukrainian Carpathians at approximately 12 Ma (Gągała et al., 2012; Nakapelyukh et al., 2018), and the Romanian Carpathians after 10 Ma (Matenco and Bertotti, 2000). The cessation of contraction in the belt has been linked to break-off of the European slab, which also propagated from northwest to southeast (Nemcok et al., 1998; Wortel and Spakman, 2000; Cloetingh et al., 2004). The slab is still attached in the southeasternmost corner of the Carpathians, known as the Vrancea Zone, where its pull on the overriding crust, in combination with the induced mantle flow, causes extremely rapid localised subsidence (Royden and Karner, 1984; Şengül-Uluocak et al., 2019). Whereas this sequence of events explains most observables, other models exist, for instance including successive panels of the slab breaking off, activating mantle cells and upwelling in the Pannonian Basin (Konĕcný et al., 2002), or including lithosphere delamination

and Neogene extension in the Pannonian realm leading to eastward extrusion of the Carpathian microplates by mantle flow
95   (Kovács, 2012).

The Carpathians consist of an inner and an outer belt. In Ukraine, most of the thick-skinned Inner Carpathian units are
covered by Neogene volcanics that erupted on the edge of the Pannonian basin; they only crop out in a limited area next to
the border with Romania. The Ukrainian Carpathians thus mainly expose the outer flysch nappes of the belt (Fig. 1); these
100   consist of a series of thin thrust sheets that contain Cretaceous to Miocene mostly deep-water clastic sediments and were
accreted north-eastward and then thrust onto the East European platform during the early to middle Miocene (Fig. 1c). Each
nappe groups several units that display similar sedimentation sequences and share the same décollement horizon (Fig. 2).
Convergence and accretion of the Carpathian wedge is thought to have started in the Oligocene in Ukraine, when the
innermost nappes of the Outer Carpathians were integrated into the accretionary wedge (Gągała et al., 2012; Nakapelyukh et
105   al., 2018).

Total convergence in the Ukrainian Carpathians is around 340 km, according to balanced cross-section restoration
(Nakapelyukh et al., 2018). Low-temperature thermochronology data combined with balanced cross-sections have been
interpreted to record two phases of shortening in Oligocene-Miocene times and out-of-sequence thrusting in both the
Western and Eastern Carpathians (Matenco et al., 2010; Merten et al., 2010; Mazzoli et al., 2010; Castelluccio et al., 2016;
110   Nakapelyukh et al., 2018). These studies postulate a slower convergence phase before the emplacement of the Outer
Carpathian nappes on the European platform followed by a rapid shortening phase with out-of-sequence thrusting during
collision. In the Ukrainian Carpathians, the slow convergence phase took place from the middle Oligocene to the early
Miocene (~32 Ma to ~20 Ma). The rapid contraction phase occurred from the early to late Miocene, with an estimated
shortening rate around 21 km/My (Nakapelyukh et al., 2018). Internal thrusting of the Inner Carpathian nappes provoked
115   contraction in the adjacent basins and propagating thrusts scraped off sediment sheets from the down-going plate,
imbricating them into the wedge. It is estimated that the Ukrainian Carpathians became quiescent at ~12 Ma, when rollback
of the European slab and foreland propagation of thrusting ended in the region (Nemčok et al., 2006).

Present-day surface heat flow in the Ukrainian Carpathians, the Pannonian back-arc basin and the European foreland is well
constrained. Heat flow in the Pannonian Basin is about 90-100 mW/m², with the highest values (~100 mW/m²) recorded
120   close to the Carpathian volcanic arc (Pospisil et al., 2006). Heat flow diminishes across the fold-and-thrust belt, from ~80
mW/m² at the contact with the innermost nappes to values between 40 and 70 mW/m² within the outer nappes (Pospisil et al.,
2006). It is possible that Middle Miocene calc-alkaline volcanic intrusions adjacent to the inner nappes, emplaced between
13.8 and 9.1 Ma (Seghedi et al., 2001), provided a transient source of heat. However, considering the small region affected
(Horvath et al., 1986), this post-collisional volcanism is unlikely to have had a major impact on heat flow in the region, in
125   line with inferences for the Transylvanian back-arc basin in Romania just to the south of our study area (Tiliță et al., 2018).

Another source of transient heat during emplacement of the Carpathian nappes may have been back-arc extension and asthenosphere upwelling under the Pannonian basin between 19 and 15 Ma (Tari et al., 1992; Horváth and Cloetingh, 1996). However, Andreucci et al. (2015) showed that heat derived from the Pannonian Basin did not affect the Carpathian nappes: low-temperature thermochronology and vitrinite reflectance data indicate a maximum paleo-temperature of 170 °C for the
130   inner part of the wedge, with temperatures decreasing from the middle part of the wedge towards the Pannonian Basin. Well data reveal that present-day geothermal gradients in the Skyba nappe range from 20 to 24 °C/km (Kotarba and ~~Kolunt~~, 2006). Due to the absence of evidence for transient heating and in line with present-day well data, an average geothermal gradient of 25°C/km for the Carpathian wedge and its antecedent basin is used in this study.

3 Stratigraphy of the Ukrainian Carpathians

135   As mentioned above, the Ukrainian Carpathians consist of a number of nappes or thrust sheets, which are differentiated based on their position, stratigraphy and tectonic evolution (Sandulescu, 1988; Oszczypko, 2006). Whereas the stratigraphy of each nappe is to some degree distinct, there are some overarching similarities. Broadly speaking, the Carpathian embayment can be treated as a passive-margin basin, subdivided by several mostly submarine ridges. As all the nappes are autochthonous from the Carpathian embayment, their stratigraphic relations retrace the convergence and evolution of the
140   Ukrainian Carpathian wedge before and during accretion. Figure 2 depicts the stratigraphy of the units containing our samples and other units useful for further interpretations. It is mainly based on the Ukrainian geological maps (Docin, 1963; Vachtchenko et al., 2003; Gerasimov et al., 2005; Matskiv et al., 2008, & 2009) with some exceptions specified below. In the region where we sampled, the Magura nappe (including the Marmarosh domain, following Oszczypko et al., 2005) contains mostly Paleogene sediments, starting with thin-bedded Paleocene flysch followed by an alternation of massive
145   sandstone beds and thin-bedded flysch in the Eocene (Fig. 2). Sedimentation stopped at the Eocene-Oligocene boundary. The Burkut and Dukla nappes display a very similar stratigraphy from the Lower Cretaceous to the upper Eocene: Early Cretaceous sedimentation started with thin-bedded flysch and limestones as well as some breccia incorporating Jurassic limestones and volcanic rocks. These are followed by sandier deposits in the Upper Cretaceous. In the Paleocene, the sedimentation evolved into a sandy flysch with conglomerate intercalations, followed in the Eocene by thin-bedded flysch
150   varying in thickness throughout the basin. Oligocene sedimentation started with argillites and limestones evolving into thick-bedded sandstones at the top of the Burkut nappe. The youngest sediments of the Dukla nappe consist of grey flysch with thick-bedded sandstones and radiolarites (known as Menilites beds), as well as olistostromes, all deposited in the Oligocene. Sedimentation in the Krosno Nappe started in the Eocene with thick-bedded flysch. The siliceous Menilites beds, which can be followed throughout the Carpathians, mark the base of the Oligocene and are followed by grey argillites and siltstones.
155   The Krosno suite was deposited from the middle-Oligocene to the early Miocene, i.e., up to the regional Eggenburgian stage (~18.1 Ma). This particularly thick unit consists of 2 km of sandy flysch sequences with intercalations of olistostromes, argillites, siltstones, and some calcareous layers.

The following nappe in the pile is the Skyba nappe. It is composed of two depositional subunits, an internal unit resembling the Krosno Nappe in the Oligocene, and an external unit in which Miocene sediments are missing. Sedimentation in both
160 subunits started in the Late Cretaceous with a sequence of thin grey flysch and marl-limestone interbeds with conglomerate lenses. The overlying Paleogene sediments are divided into four suites, alternating between thick-bedded sandstones and thin-rhythmic flysch with conglomerate lenses at the base. These were followed in the Oligocene by the Menilites beds which evolved into calcareous argillites, grey sandstones with black argillites, and thin sandstones with grey carbonaceous argillites for the internal units. This is topped by Miocene grey argillites with siltstone interbeds deposited until the end of
165 the Eggenburgian (18.1 Ma) in the internal unit. For the external unit, Oligocene deposits, including the Menilites beds, are followed by marls and coarse layered batches of sandstones (Oszczypko, 2006).

Sedimentation in the Boryslav-Pokuttia nappe began in the Late Cretaceous with argillites intercalated with limestones as well as with some conglomerate lenses. In the Palaeocene, thick sandstones were deposited, followed by an Eocene alternation between thin and thick-bedded flysch deposits. The Oligocene Menilites Beds are overlain by sandstones with
170 calcareous siltstones. From the early Miocene to the end of the Eggenburgian, the Boryslav-Pokuttia nappe accumulated siltstones and clays evolving into thin sandstones, with intercalations of clay. There are also some lenses of conglomerates. A thick layer of argillites and siltstone with lenses of salt was deposited on the nappe during the Ottnangian (18.1-17.2 Ma, Fig. 2). After this time, sedimentation extended onto the Sambir nappe. While argillites with thin sandstone interbeds accumulated on the Boryslav-Pokuttia nappe, conglomerates and sandstones were deposited on the Sambir nappe
175 (Andreyeva-Grigorovich et al., 2008). Sedimentation stopped at the end of the early Miocene on Boryslav-Pokuttia, apart from several tens of metres of conglomerates thought to be Pliocene in age. Thick deposits of clay and marls evolving into tuffites and salt accumulated, on the other hand, on the Sambir nappe during the Middle Miocene, where deposition continued to the end of the early Sarmatian (10.7 Ma); the remaining Miocene deposits are syn-tectonic conglomerates dated around 9 Ma (Andreyeva-Grigorovich et al., 2008).

4 Methods

4.1 Low-Temperature Thermochronology

Low temperature thermochronology can record the thermal evolution of mountain belts and the exhumation of rock in the crust over a large range of temperatures ($30 - 300$ °C), corresponding to depths of 1-10 km for a normal geothermal gradient (e.g., Ault et al., 2019). Here we use the apatite fission-track (AFT) and apatite (AHe) and zircon (U-Th-Sm)/He (ZHe) low-
185 temperature thermochronometers. These have nominal closure temperatures in the range of 80-120 °C, <80 °C, and <200 °C, respectively, depending on cooling rate, mineral composition and accumulated α-damage (e.g., Ault et al., 2019). When these methods are applied to sedimentary rocks (i.e., in detrital thermochronology), they either record information on the pre-depositional history of the deposits, or on their post-depositional burial and subsequent exhumation, depending on the

maximum burial temperature experienced by the samples (e.g., van der Beek et al., 2006; Fillon et al., 2013). In a flysch
190   basin, detrital grains are derived from a variety of source rocks and therefore tend to show a wide range of chemical
compositions and apparent cooling ages, if they were not affected by full thermal resetting during burial heating. Thus,
detrital thermochronology potentially allows tracing both the pre- and post-depositional history of the sampled sedimentary
rocks, if a sufficient number of grains can be analysed per sample (e.g., van der Beek et al., 2006; Fillon et al., 2013). The
combined thermochronological data can also be used for thermal-history modelling (see section 4.2.1).

195   **4.1.1 Sampling**

Fourteen samples, weighing 3-5 kg each, were collected from sandstones across three transects in the Ukrainian Carpathians
(Table 1). Sampling focused on areas that were not targeted in previous studies (Andreucci et al., 2015; Nakapelyukh et al.,
2018), aiming to collect at least one sample per tectonic unit along each transect (Fig. 1). Samples were crushed and sieved,
after which apatite and zircon were separated from other minerals with standard heavy-liquid and magnetic separation
200   techniques. Apatite grains were hand-picked under the microscope for subsequent apatite fission-track (AFT) and apatite (U-
Th-Sm)/He (AHe) dating. Zircon (U-Th-Sm)/He (ZHe) dating was performed on the same samples. Most samples yielded
sufficient apatite and zircon grains for all three analyses, but in some of the samples, one or two of the analyses were not
possible (Table 1).

4.1.2 Fission-track thermochronometry

205   Eleven samples were prepared for apatite fission-track thermochronometry at the GTC (Geo-Thermo-Chronology) platform
of ISTerre, Grenoble (France) using the external detector method (Hurford and Green, 1982). Apatite crystals were mounted
in resin, polished and etched with a 5.5M HNO_3 solution at 21°C during 20 s, and attached to a mica detector. The mounted
apatite crystals were irradiated at the Oregon State University Triga reactor (USA). Ten samples contained sufficient
countable grains for statistically meaningful dating; AFT ages were only calculated for samples with more than 30 counted
210   grains. Three Durango and three Fish Canyon Tuff standards were used to determine a ζ-calibration value of 282±12 yr.cm^{-2}.
Etch-pit width (Dpar) measurements were made on each analysed grain in order to determine compositional variations in the
apatites, which are known to have an influence on their kinetics (e.g., Carlson et al., 1999).

4.1.3 (U-Th-Sm)/He thermochronometry

Fracture- and inclusion-free apatite and zircon grains were picked under a microscope; their size was measured and their
215   shape recorded. Of the 11 samples considered, 10 contained apatite and zircon suitable for (U-Th-Sm)/He dating, with one to
five single grains of apatite/zircon per sample dated (Tables 3 and 4). ^{4}He concentrations were measure at the University of
Potsdam (Germany): crystals were encapsulated and heated by a laser to extract ^{4}He; after mixing with a known amount of
purified ^{3}He gas, the gas mixture was analysed in a quadrupole noble-gas mass spectrometer. The crystals were dissolved

and their U, Th and Sm content determined by ICP-MS at the German Research Centre for Geosciences (GFZ) Potsdam
220   (Germany) following the methodology of Galetto et al. (2021) and Zhou et al. (2017). AHe and ZHe ages were corrected for
α-ejection using the methods outlined by Ketcham et al. (2011).

4.2 Time-temperature models and tectono-stratigraphic analysis

4.2.1 Thermal history modelling

We modelled the time-temperature (T-t) pathways constrained by one or more samples for each of the nappes using the
225   QTQt (version 5.8.0) code (Gallagher, 2012), which employs a Markov chain Monte Carlo inversion method. Inputs for the
modelling consisted in our ZHe, AHe, and AFT dates, Dpar values and depositional ages, as well as a limited number (<20
per sample) of fission-track lengths and angles to the c-axis. We used the diffusion model of Gautheron et al. (2009) for AHe
and that of Guenthner et al. (2013) for ZHe, as well as the multi-kinetic annealing model of Ketcham et al. (2007) for AFT.
For all models we explore a temperature range of 0-300°C and a time range of 350-0 Ma. We included a maximum of two
230   constraints when exploring the T-t space: (1) samples should reside at surface temperatures (5±5 °C) at the depositional age
of their host sediment; (2) we imposed a 150±50 °C temperature constraint at 150±50 Ma for the samples belonging to the
Magura, Burkut and Dukla units. The latter was applied to force a (partial) reset of the ZHe system in these units before
calculation of the burial temperatures after deposition, i.e., the scenario that best complies with our thermochronological
results (see below). Inversions were run with 100.000 models for the burn-in and 150.000 models for the post burn-in
235   phases. Model outcomes include a probability field for the range of thermal histories explored as well as several alternative
"best-fit" models: The maximum likelihood model is the one that fits the input data the best out of all the burn-in and post-
burn-in models, while the "maximum post" model is the post-burn-in model that best fits the data; both may show
unwarranted structure, however (Gallagher, 2012). We therefore prefer the "expected" model, which reflects the average of
all the tested models, weighted by posterior probability, and its 95% credibility interval to indicate the most probable thermal
240   history recorded by our samples.

4.2.2 Tectono-stratigraphic analysis

The stratigraphy of the wedge (Fig. 2) contains important information on the pre- and syn-orogenic evolution of the
Ukrainian Carpathians: the age, thickness, lithology, depositional environment and provenance of the corresponding
sediments provide insight into the former topography and tectonic activity in the region. To complete the post-depositional
245   thermal history, we therefore compiled sedimentary burial diagrams for each sampled unit, using the stratigraphy published
on the 1:200,000-scale geological maps of the Ukrainian Carpathians (Docin, 1963; Vachtchenko et al., 2003; Gerasimov et
al., 2005; Matskiv et al., 2008 & 2009), which is compiled in Fig. 2. It is notoriously difficult to date flysch deposits, which
contain much reworked fauna, and deformation clearly complicates stratigraphic measurements in the wedge, but keeping

this in mind, the stratigraphic data nevertheless provide a useful complement to the thermochronological results. The burial
250 diagrams in Fig. 2 indicate to which minimal depth samples were buried by sediment accumulation, when the sedimentation
rates of the nappe changed, and give a maximum age for cessation of sedimentation. Combined with the thermal history
models, this information allows discriminating sedimentary from tectonic burial, and tracking the full burial-exhumation
cycle for each nappe. As we are mainly interested in the timing and amount of maximum burial, we made no attempt to
correct the burial curves for compaction effects. Sedimentary thicknesses shown in Fig. 2 are averaged for each tectonic unit,
255 resulting in some uncertainty in the thickness of the sedimentary overburden for our samples that can be substantial and
increases with progressive burial.

5 Results

5.1 Apatite Fission-Track ages

AFT data are reported in Table 2 and Fig. 3. All samples are characterized by significant age dispersion and $P(\chi^2)$ values
260 close to zero, indicating that they contain multiple age populations. This may be explained by inheritance of a wide variety
of detrital grains in our sandstone samples in combination with partial resetting as a result of relatively low temperatures
experienced since deposition. In our dataset, samples CAR19-056, -062, -063 and -068 are relatively close to full resetting,
as nearly all single-grain ages are younger than the depositional age (Fig. 3). The rest of the samples contain a large
proportion of grains that are significantly older than, or in the range of, the depositional age.
265 When dealing with significantly dispersed single-grain ages such as here, central ages (Fig. 3, CA) are not geologically
meaningful. We therefore used the RadialPlotter program (Vermeesch, 2009) to determine major grain age components
(peaks), applying the mixture modelling algorithm of Galbraith and Green (1990), as well as the minimum age (Galbraith
and Laslett, 1993) for each sample. Between one and three age peaks were detected in our AFT age distributions (Fig. 3).
The youngest peak (P1) generally corresponds within error with the calculated minimum age component (Fig. 3).
270 Minimum ages for samples from the Magura Nappe (CAR19-061, -066) range from 24.0 ± 3.3 to 31.0 ± 3.7 Ma, indicating
cooling of this nappe possibly before the Miocene (Fig. 3). Samples CAR19-062, 063 and 068 from the Burkut and Dukla
nappes are strongly reset and have very similar minimum ages of 11.0 ± 3.0 Ma, 11.0 ± 1.5 Ma, and 10.0 ±1.5 Ma
respectively (Fig. 3). These minimum ages are also similar to the 11.0 ± 0.9 Ma minimum age of sample CAR19-069 from
the adjacent Krosno nappe, which is partially reset. The minimum age of sample CAR19-070, which derives from a more
275 external position on the Krosno nappe, is 13.0 ± 4.4 Ma. Samples CAR19-045 and 056 from the Skyba nappe display
minimum ages of 21.0 ± 2.4 and 16.1 ± 1.0 Ma respectively, the latter being strongly partially annealed. Sample CAR19-
072, which comes from the same nappe, shows a younger but less precise minimum age of 12.0 ± 6.6 Ma.
In summary, the Magura nappe has partially reset populations with Oligocene minimum AFT age, the Burkut and Dukla
nappe have strongly partially annealed age distributions with late Miocene minimum ages, whereas the Krosno and Skyba

280   nappes have partially reset age populations, with minimum ages that generally fall into the early to middle Miocene, except for the innermost part of the Krosno nappe which has a late Miocene minimum age, more similar to the Brukut and Dukla nappes.

5.2 Apatite (U/Th)/He ages

AHe dates are reported in Table 3 and Fig. 4. Whereas some samples (CAR19-056, -068, -069) show overlapping middle-
285   late Miocene single-grain AHe ages, most samples have widely dispersed ages without a clear correlation with effective Uranium content (eU) or grain size (Supplementary Data Table S1). Although this is to be expected in detrital samples where grains are characterised by differences in size, eU, as well as pre-depositional thermal history (e.g., Fillon et al., 2013), there are a few single-grain ages that need to be treated with caution. We suspect He loss to have caused anomalously young single-grain ages in samples CAR19-047 and CAR19-62 (Table 3), which we do not consider further. Older AHe ages are to
290   be considered taking into account partial resetting of the AHe system, given the potentially large diversity of radiation damage, grain size and pre-depositional history. This can be the case for samples CAR19-061, -062, -066 and -072, which all have grains with either Paleogene or Miocene AHe ages. We find a relatively large spread of AHe grain ages in the Magura and Burkut nappe samples (respectively CAR19-061, -066, -062 and -063). In contrast, samples from the Dukla, Krosno and Skyba nappes, with the exception of CAR19-072, show less age dispersion in the AHe system. If we do not take into account
295   the AHe ages that are older than the minimum AFT ages of the respective samples, and are therefore clearly partially reset, we find two prominent age peaks in our data: one at 13.5 ± 2.0 Ma and one at 8.8 ± 2.0 Ma. These comprise 70% of the data.

5.3 Zircon (U/Th)/He ages

Zircon (U/Th)/He data are reported in Table 4 and Fig. 5. All but three of the single-grain ages are older than the
300   depositional age of the samples and thus non-reset. Single-grain ages show little correlation with eU or grain size (Fig. A1). The three grains with young ZHe ages (two in sample CAR19-045 and one in CAR19-056) also have suspiciously low U and Th contents and anomalous U/Th ratios (Table 4). A grain from sample CAR19-069 has a ZHe age that is only slightly older than the depositional age and similar characteristics, while a grain from sample CAR19-072 also has very low U and Th content, even though its ZHe age is significantly older than the depositional age. We do not include these grains in our
305   further discussion.

Two clear populations of ZHe ages can be discerned in the remaining grains: 60-130 Ma ZHe ages were obtained from samples from the inner nappes (Magura/Marmarosh, Dukla, Burkut, Krosno) and 230-450 Ma ZHe ages from the outer nappes (Skyba, Boryslav-Pokutia). Because the ZHe ages are demonstrably non-reset, these age groups likely relate to different provenance areas for the detrital zircons in these units.

5.4 Thermal-history models and tectono-stratigraphy

310

We modelled time-temperature histories for eight samples and briefly summarize the results below, going from the internal to the external nappes. The depositional age of sample CAR19-066, from the Magura Nappe, is Lutetian-Bartonian (48-38 Ma; Matskiv et al., 2008). After deposition, it underwent 800±400 m of sedimentary burial until the end of the Eocene (34 Ma). Thermal-history modelling indicates that the sample reached its peak temperature of 85-105 °C around 24-18 Ma, i.e.

315 more than 10 My after the end of sedimentation on the nappe (Fig. 6). The sample subsequently cooled at a constant rate until the present day. There are two interpretations of the stratigraphy of the laterally equivalent Marmarosh Nappe (cf. Oszczypko et al., 2005; Matskiv et al., 2009), which influences the inferred amount of burial, but not the depositional age of the corresponding sample CAR19-061. After deposition in the Bartonian-Priabonian (41-34 Ma), the sample underwent 800±200 m of pre-Oligocene burial according to the geological map (Matskiv et al., 2009), whereas ~500 m of additional

320 sedimentary burial is inferred based on the Oszczypko et al. (2005) stratigraphy (Fig. 6). Time-temperature modelling of sample CAR19-061 suggests rapid syn- and post-burial heating to a 85-100 °C peak temperature, which was reached around 31-29 Ma, with continuous cooling, at a constant rate, starting ~4 My after sedimentation ended.

Next in the direction of vergence of the belt is the Burkut nappe, from which samples CAR19-062 and CAR19-063 were modelled (Fig. 7). Sample CAR19-062 has a Cenomanian-Turonian depositional age (102-89 Ma) and shows a long burial

325 phase under a total of 4000-5000 m of sediment (Matskiv et al., 2009); sedimentation on the nappe ended in the mid-Oligocene (ca. 28 Ma). Thermal-history modelling reveals a correspondingly long heating phase, with the peak temperature between 105 and 125 °C being reached around 40 Ma. The onset of cooling is difficult to pinpoint exactly for this sample, but the 95% credible intervals of the expected model show a clear cooling step at ~17.5 Ma. Subsequent cooling was intermittent, with a possible acceleration after 10 Ma (Fig. 7). Sample CAR19-063 has a Danian-Ypresian (65.8-47.8 Ma)

330 depositional age and was buried under 2000-3000 m of sediment until the mid-Oligocene (ca. 28 Ma) (Matskiv et al., 2009). Thermal-history modelling indicates that sample CAR19-063 reached a maximum temperature of 110 to 155 °C at 23-18 Ma and began cooling immediately after. Cooling possibly slowed down at around 10 Ma.

Sample CAR19-068 was modelled to retrieve a thermal history for the Dukla nappe (Fig. 8). After deposition in the Campanian-Maastrichtian (83.6-66 Ma), ~3000 m of sediments accumulated on top of the sampled sandstone until the mid-

335 Oligocene (ca. 28 Ma) (Matskiv et al., 2008). Thermal-history modelling indicates that heating lasted some 8 My longer; the sample reached a peak temperature of 100 to 130 °C at 13±2 Ma, followed by rapid cooling at a constant rate.

Sample CAR19-069 is from the Krosno Nappe and was deposited in the Chattian (28-23 Ma). It subsequently rapidly accumulated an overburden of 2500±500 m. Sedimentation on the nappe terminated in the Early Miocene (Eggenburgian; ~18 Ma; Matskiv et al., 2009). Thermal-history modelling indicates that the peak temperature of 115°C was reached shortly

340 after (~17 Ma), followed by continuous and rapid cooling.

The outermost nappe for which we derived thermal-history models is Skyba. Sample CAR19-045 was deposited in the Lutetian-Bartonian (48-38 Ma; Vachtchenko et al., 2003) and accumulated an overburden of 1700±400 m of sediments until

the Burdigalian, when sedimentation on the nappe stopped. Thermal-history modelling retrieves a most likely onset of burial
heating at ~45 Ma and a maximum temperature of 85-100 °C that was reached at 12±1 Ma (Fig. 9). Subsequent cooling was
345   rapid and continuous until the present. Sample CAR19-056 was deposited in the Turonian-Danian (94-62 Ma; Docin, 1963)
and accumulated 4000-5000 m of sediment until the Early Miocene (Eggenburgian, ~18 Ma). Thermal-history modelling
reveals both syn- and post-depositional heating from ~68 Ma to ~16 Ma, up to a maximum temperature of ~120 °C, followed
by rapid and continuous cooling to the present.

6 Interpretation and Discussion

350   ### 6.1 Burial and exhumation pathways in the Ukrainian Outer Carpathians

The burial diagrams and time-temperature models for the various nappes of the Ukrainian Carpathians obtained in our study
provide enhanced insight into the evolution of the orogenic wedge. For several of our samples (CAR19-045, 061, 066, 063,
and 069), the peak temperature encountered during burial is very high when compared to the temperatures that would result
from sedimentary overburden alone. Moreover, some samples show continued heating after sedimentation on the nappe had
355   terminated, requiring another process to explain this additional heating. We infer that each nappe experienced a tectonic
burial phase after the end of deposition, which imbricated the sediment into the wedge and/or thrusted more internal nappe
units onto the sedimentary column. Burial diagrams generally reveal that sedimentation stopped several million years before
cooling of the nappe commenced. We interpret this to reflect that sedimentation stopped when accretion of the nappe started.
The amount of additional heating after the end of sedimentation, as well as the time lag between the end of sedimentation
360   and the onset of cooling, reflect the relative importance of tectonic thickening due to thrusting, and surface erosion (Husson
and Moretti, 2002; Ter Voorde et al., 2004).
To estimate how much tectonic burial a sample underwent, we estimate a geothermal gradient of 25°C/km for the evolving
wedge (Section 2; Kotarba and Kolunt, 2006). This allows us to translate the modelled time-temperature paths, based on the
thermochronological data, into depths of burial. We note that this approach neglects heat advection and blanketing effects
365   during burial and exhumation. Inferred cooling rates for our samples are all ≤10 °C/My, leading to maximum exhumation
rates of 400 m/My using the estimated geothermal gradient (see below). Maximum burial rates are significantly lower than
that, <200 m/My for all samples and in the range 50-70 m/My for most of them. Such burial and exhumation rates, combined
with a detachment depth of 10-15 km (Fig. 1) are not expected to significantly perturb the conductive thermal structure of
the fold-and-thrust belt (Husson and Moretti, 2002; Braun et al., 2006). The evolving topography of the wedge could also
370   have affected the thermal structure recorded by in particular the lower-temperature thermochronometers AFT and AHe (e.g.,
Braun et al., 2006). As the topographic evolution of the Ukrainian Carpathians is currently unconstrained, we neglected this
effect. The resulting burial and exhumation paths are thus first-order approximations of the evolution of the wedge.

The amount and timing of sedimentary burial, as derived from the nappe stratigraphy, is indicated in the burial diagrams. The amount and timing of tectonic burial can thus be found by subtraction of this amount from the maximum burial inferred

375 from the time-temperature path. The results are shown in Fig. 11. As seen in the regional cross section in Fig. 1, internal thrusting affects each nappe, thus the time-depth model represents only one internal thrust slice. Nevertheless, we consider the whole nappe to have behaved more or less according to the thermal models. Finally, assuming that cooling of the sample from the maximum depth of burial to the present-day surface occurred by erosional unroofing, exhumation rates can be calculated for the different nappes of the wedge. This also allows calculation of the total amount of eroded sediment per

380 nappe. Modelled thermal histories can thus be interpreted in terms of sedimentary and/or tectonic burial and subsequent exhumation of the nappe (or unit) they belong to. We use the mean expected model as the reference for all interpretations of sample pathways. Interpretation of the modelled thermal histories provides information on the evolution of the Ukrainian Carpathian wedge and highlights the different stages of tectonic burial and final exhumation of the wedge (Fig. 11).

The Magura and Marmarosh nappes were accreted at approximately 34 Ma and had a stage of tectonic burial that lasted to

385 30 Ma in the SE and to 20 Ma in the NW (according to sample location) that brought the rocks 2.5-3 km deeper than the prior sedimentary burial. Subsequent exhumation amounted to ~4 km, at rates of 0.12-0.14 km/My and 0.16-0.22 km/My, respectively.

Accretion of the Burkut nappe occurred at ~28 Ma for both samples (CAR19-063 and CAR19-062) and tectonic burial brought them respectively to 5.0 and 5.5 km depth. The following exhumation stage occurred in two phases: a first phase

390 between 18-10 Ma and a second phase after 10 Ma. The two samples from this nappe have different exhumation rates before 10 Ma (0.22 km/My for CAR19-062 and 0.40 km/My for CAR19-063); however this difference may be linked to the lack of time constraints on the peak burial and the initiation of the exhumation stage (especially for CAR19-062), as the timing of the peak temperature impacts directly exhumation rate estimation, which is interpolated from the peak to the next inflexion point of the cooling path. However, the post-10 Ma exhumation rate is ~0.3 km/My for both samples and the thickest

395 overburden (up to 5.5 km) was eroded from this nappe. The Dukla nappe shows a long tectonic burial stage, from ~28 Ma to 14 Ma, and started exhuming later than the Krosno and Skyba nappes, which are in a more external position. This timing suggests out-of-sequence thrusting in the Dukla nappe, in line with inferences by Roure et al. (1993). Exhumation of the Dukla nappe started around 12 Ma and occurred at a rate of ~0.38 km/My.

The samples of the Krosno nappe (CAR19-069) and the north-west part of the Skyba nappe (CAR19-056) display very

400 similar thermal histories, with a stage of tectonic burial (i.e., accretion) starting at 18 Ma, preceded by rapid syn-orogenic sedimentation on the Krosno nappe (Fig. 2; Shlapinskyi, 2015; Nakapelyukh et al., 2018). Their exhumation started not long after, at respectively ~17 and ~16 Ma. The southeast part of the Skyba Nappe (sample CAR19-045), on the other hand, continued its tectonic burial until 12 Ma. Exhumation rates for the Krosno and Skyba nappes were around 0.3-0.4 km/My and 4-5 km of overburden was removed at a significantly higher rate than that of the other Middle nappes. We have no

405 thermal history models for the Boryslav-Pokuttia and Sambir nappes due to their much lower heating, below the level of

AFT partial annealing. However, deposition ~~on~~ the Boryslav-Pokuttia ~~Nappe~~ continued until 17.2 Ma (Andreyeva-Grigorovich, 2008), while AHe data indicate exhumation at 12.8-9.5 Ma.

We thus see an apparent increase of exhumation rates from the inner to the outer nappes in our models. However, this could simply be related to the later time of peak burial in the outer nappes, as the lack of track-length measurements lowers the
410 resolution of the thermal history at shallow depths, potentially failing to resolve earlier exhumation to the surface of samples in the inner nappes.

6.2. Evolution of the Ukrainian Carpathian wedge

Our combined tectono-stratigraphic and thermochronological analysis allows us to identify several sedimentary and tectonic events and to retrieve the activity of Ukrainian Carpathian wedge over time. We outline and discuss our main observations of
415 the different stages below.

Several nappes show an increase in sedimentation rate before the onset of the accretion phase (marked by tectonic burial) of successive parts of the antecedent basin (Fig. 11). Such increasing sedimentation rates are expected in a pro-foreland basin adjacent to an approaching frontal thrust (Naylor and Sinclair, 2008), as also suggested for the Polish Carpathians (Oszczypko, 2006; ~~Poparwa~~, 2002). In the Magura nappe, sedimentation ended in the Eocene and depositional rates
420 increased in the early-middle Eocene, especially in the Marmarosh Unit (Fig. 2). In the Burkut and Dukla ~~nappes~~, sedimentation ended in the middle Oligocene; the approach of the active front toward these nappes is reflected by a coarsening of the grain size and olistostromes in the flysch without a marked acceleration of the sedimentation rate. For the Krosno nappe, the two-kilometres-thick sandstones show a rapid increase in sedimentation rate within the basin starting in the late Oligocene, probably due to increased accommodation space in combination with high sediment supply.
425 Sedimentation in the proximal units of the Skyba nappe is similar to the Krosno nappe, with Oligocene sandstones and Miocene syn-orogenic sediments. More distal units of Skyba contain only ~~late~~ Oligocene sediments and Miocene layers are absents, either because of erosion of the strata, or by underfilling of the basin in the early Miocene with deposition on basin lower points, or due to the lower plate flexure with an advancing deformation front. The Boryslav-Pokuttia and Sambir nappes accumulate the majority of their deposits in the Miocene, with levels of sandstones (and olistostromes), followed by
430 evaporites lenses and fossil-rich clays, marking the evolution of the environment to a shallow sea, located in front of the wedge in the Middle Miocene (Fig. 2).

We observe diachronous building of the wedge with periods of increased tectonic activity. For the Magura nappe, the onset of accretion is at 34 Ma and exhumation is between 30-22 Ma, coeval with the accretion of the Burkut and Dukla nappes (around 28-22 Ma). Exhumation of the Burkut nappe started immediately afterwards at ca. 20 Ma and the next nappes in
435 line, Krosno and Skyba, were being accreted at 18 Ma. Onset of exhumation occurred shortly after for the Krosno nappe, whereas it occurred around 12-8 Ma on the Skyba nappe. Out-of-sequence thrusting in the wedge also occurred during this period, with the onset of the exhumation of the Dukla nappe at 14 Ma. A basement high was inferred from an analysis of

exotic rocks present in the flysch (Shlapinskyi, 2007; Nakapelyukh et al., 2018), but in an initial position under the adjacent Dukla nappe. We suggest this basement block was located under the Krosno nappe in the northwest of the Ukrainian

440 Carpathians, as the sedimentation there started in the Paleocene, whereas toward the southeast, where sedimentation on the Krosno nappe commenced in the Mesozoic, in analogy with the adjacent Dukla and Skyba nappes, the ridge may have disappeared. The ridge may correspond to the sub-Silesian ridge recognised in Poland (Oszczypko, 2006). The corresponding basement block is resolved by geophysical measurements in a current position under the internal part of the Carpathians (Zayats et al., 2013). The arrival of this basement high at the subduction zone may have given rise to the

445 formation of duplexes and out-of-sequence thrusting in the Dukla nappe (Roure et al., 1993; Nakapelyukh et al., 2018). Apart from some minor Pliocene conglomerates, the youngest deposits on the Boryslav-Pokuttia nappe are 17.2 Ma (Fig. 2), with local deposits on the outskirt of the nappe dated at 13.5 Ma according to Andreyeva-Grigorovich 2008, which indicates that it was buried tectonically in most part after 17.2 Ma but with local (syn-tectonic ?) deposition around 13.5 Ma. This was the last stage of foreland-propagating thrusting that we can resolve. The nappe was exhumed at the same time as the Skyba

450 nappe, as marked by its late Miocene AHe ages (12.8 ± 0.2 Ma and 9.5 ± 0.1 Ma). During this last stage, the wedge was thrust over the Sambir nappe and onto the East European Platform corresponds to the halting of foreland propagation (11.5 Ma) of the frontal thrust in the Ukrainian foreland (Nemčok et al., 2006; Nakapelyukh et al., 2018).

6.3 Thermochronometric pattern and wedge dynamics

In line with previous data, our results reflect partial resetting of the AFT system and fully reset AHe ages in the central

455 nappes (Fig. 10). We find strong partial annealing of the AFT system and full resetting of the AHe system in the Burkut and Dukla nappes, and Andreucci et al. (2015) provide evidence for (strong) partial resetting of the ZHe system. In contrast, the AHe and AFT systems are partially reset, and ZHe is non-reset in the innermost Magura nappe. For the more external Krosno and Skyba nappes, AFT samples are variably reset, with less resetting in the outer parts of these nappes. AHe ages, on the other hand, are fully reset in the Krosno nappe. The external part of the Skyba Nappe reveals non-reset AHe ages,

460 while the Boryslav-Pokuttia Nappe has some reset AHe ages. This pattern of low-temperature thermochronology ages, showing burial heating to maximum temperatures in the core of the wedge (Fig. 10) and decreasing toward both the internal and external limits, is consistent with models of steady-state orogenic wedges (Barr and Dahlen, 1990; Batt et al., 2001; Willett and Brandon, 2002). It is also comparable with exhumation patterns in other orogenic wedges, including the Olympic Mountains (Brandon et al., 1998; Batt et al., 2001); Taiwan (Beyssac et al., 2007) and the Apennines (Thomson et al., 2010;

465 Erlanger et al., 2022). The increasing thermochronometer ages toward the innermost Magura nappe may indicate that the latter acts as a relatively stable backstop (e.g., Brandon et al., 1998) or that the Ukraine Carpathians constitute an "immature" wedge, where steady state has not been reached sufficiently long to exhume reset thermochronometers on the nner wedge (e.g., Willet and Brandon, 2002).

In a theoretical view of wedges, the accretion of nappes should decelerate over time, i.e., accretion and frontal-thrust
470   propagation should occur with a longer period of quiescence between events as the wedge grows (Naylor and Sinclair,
2007). This does not correspond to our model results. We can infer from what we see in our time-depth diagrams (Fig. 11),
that the accretion-exhumation phases are shorter in the period between 22-18 Ma when the main nappes (Burkut, Dukla,
Krosno and Skyba) were accreted and started to be exhumed for some (see 6.2.). The geodynamic context of this orogen may
explain the observed discrepancy. In the Carpathians, the main driver of convergence is the retreat of the subduction zone
475   linked to slab roll-back in the latest stages (Royden and Karner, 1984; Royden, 1993; Wortel, 2000; Koněcný et al., 2002).
Within this context, orogenic building is ruled by the dynamics of the slab and, therefore, we infer that dynamic equilibrium
of the orogenic wedge could have been impeded by the competition between the accretion of material and the retreat of the
orogenic front due to slab roll-back, allowing no time for topography building, thermal re-equilibration or internal
deformation. In conclusion, the Ukrainian Carpathians record the competition of orogenic wedge growth and subduction
480   retreat by slab roll-back.

6.4 Sediment provenance from ZHe ages

While the reset and partially reset AFT and AHe thermochronometers provide insight into the sedimentary and tectonic
evolution of the wedge, the non-reset ZHe ages may provide insight into the sediment supply to the evolving wedge and its
485   precursor deep-water basin (Fig. 12). ZHe ages of this study can be divided in two groups containing ages of 60-130 Ma and
230-450 Ma, respectively. The younger age group is mainly found in the inner nappes of the UC (samples CAR19-061, -062,
-063; Fig.s 4, 12), while the older ZHe age population (230-450 Ma) is present in the outer nappes of the Ukrainian
Carpathians (samples CAR19-045, CAR19-047 and CAR19-056; Fig.s 4, 12). This pattern is consistent with previously
published ZHe ages from Andreucci et al. (2015), that are reset and partially reset in the core of the orogenic wedge (i.e.,
490   Burkut and Dukla nappes). But which are still unreset and younger in the inner part of the wedge, notably in the Magura
nappe, and older in the Skyba and Boryslav-Pokuttia nappe. We evidently exclude reset and partially reset ZHe ages in the
core of the orogenic wedge (i.e., Burkut and Dukla nappes) and on the Krosno nappe from this provenance analysis.
We infer that the sources of the sediment in the inner nappes, which bear mostly 60-130 Ma unreset ZHe ages, are the
Bucovinian units of the Inner Carpathians (basement units of the Dacia plate; Sandulescu, 1988; Schmid et al., 2008) and
495   their sedimentary cover. ZFT studies in the Infrabucovinian units, located in the Maramures mountains, show fully reset ages
from a cooling phase starting in Cenomanian times (~100 Ma), with another cooling event in the Coniacian-Campanian (90-
72 Ma; Gröger 2006). Sedimentation on the Bucovinian units stopped in Barremian times (129-125 Ma; Krautner, 1975) and
the onset of thrusting is dated as Aptian-Albien (125-101 Ma) by the discordant deposition of the Wildflysch formation on
top of both units (Sandulescu, 1975). For the Bucovinian and Sub-bucovinian units, which structurally overlie the
500   Infrabucovinian unit, the ZFT system is generally partially reset depending on the tectonic overburden and position in the

stratigraphy (Gröger et al., 2008). The ZFT ages from the Bucovinian units are very similar to our ZHe ages for the innermost nappes, suggesting that the source for the Magura and Burkut samples were possibly the Bucovinians units, or their Ukrainian equivalent. Sediment provenance analysis in the Western Carpathians also shows that the Magura nappe received sediments from these inner units (Winkler and Slaczka, 1992) and paleocurrent were retrace to bring sediments

505   from the Silesian ridge in the NW to the Krosno basin (Oszczypko, 2006).

We moreover infer that sediments in the outer nappes of the Ukrainian Carpathians, which contain the older ZHe age population (230-450 Ma), were sourced from the intra-basinal ridges of the East European margin, where the last exhumation phase occurred during Tethyan rifting (300-250 Ma; Winkler and Slaczka, 1992; Oszczypko et al., 2006; Schmidt et al., 2008), and from the Trans-European Suture Zone (TESZ) or the East European Craton, which contain

510   Variscan faults that were also active during the late Ordovician (~450 Ma; Pharaoh, 1999). The westernmost samples of these outer nappes (CAR19-066, CAR19-068, CAR19-069 and CAR19-072; Fig.s 4 & 12) contain a mix of the young and old age populations and were thus probably derived from both previously mentioned sources.

6.5 Sediment recycling in the Carpathian Wedge and sediment supply to the pro-foreland basin

Recycling of sediments is a major process in fold-and-thrust belts; quantifying the amount of eroded material and the timing

515   of erosion can help retrieve sediment fluxes over time. Our study provides a view on the sediment fluxes in the Ukrainian Carpathian wedge from the classic model of a formerly accreted nappe providing sediments to the next accreted nappe. Accretion and onset of exhumation of the innermost Magura nappe (34-24 Ma) happened earlier than for the rest of the wedge. However, the middle nappes were all accreted and started their exhumation in a 4-My time interval (22-18 Ma). The sediment that accumulated on these nappes before their accretion cannot have been sourced exclusively from the early thin-

520   skinned wedge, as the amount of material exhumed from the inner nappes at that time was insufficient. Multiplying the amount of exhumation of the Magura nappe in the 30 Ma to 26 Ma time-intervals with its width as shown on balanced cross sections (Nakapelukh et al., 2017; Nakapelyukh et al., 2018) and comparing this with the thickness of sediments deposited over the width of the remaining flysch basin, we find that the amount of eroded overburden from the wedge that took part in the sediment accumulated in the pro-foreland was of 5% between 30 and 26 Ma, and increase further to 13% between 26 and

525   20 Ma. This suggests that much of the syn-orogenic sediment arriving in the middle part of the basin was derived rather from the overriding plate, which is also indicated by the ZHe ages as discussed above, and from paleocurrents arriving from the NW Polish intra-basinal ridges (the Silesian ridge) supplying mostly Krosno and Skyba nappe and from the East European margin by large deltaic fan for more external nappes (Oszczypko, 2006; Popadyuk et al., 2006). The Boryslav-Pokuttia nappe received little sediments after 17.2 Ma, despite some local deposition on the outskirt of the unit around 13.5 Ma (Fig.

530   2; Andreyeva-Grigorovich, 2008). However, the middle nappes at that time had mostly started their exhumation phase, hence a large part of the eroded sediments from the wedge was transported or remobilised into the Sambir nappe and the modern Carpathian foreland basin (Fig.s 2, 13). In fact, the tectono-stratigraphic analysis, in combination with the kinematics of the

Ukrainian Carpathians, indicates very little sediment recycling between the nappes, but rather suggests a large-scale by-pass

of the sediment directly to the most external nappe (i.e., Sambir) after the Ottnangian (18.1–17.2 Ma), and to the foreland

535 after 12-8 Ma.

7. Conclusion

This study adds constraints on the construction of the Ukrainian Carpathians through low-temperature thermochronology.

AFT and AHe single-grain ages show partial resetting in the most internal and external nappes and a progression to a very

strong partial reset and total reset with young AHe ages (8-6 Ma) and young minimum AFT ages (16-8 Ma) in the central

540 nappes (Burkut and Dukla). ZHe dating shows mainly non-reset grains, except for the central part of the wedge, and marks

exhumation of the sediment source areas for the different basins. The distribution of ZHe ages indicates a southwestern

source for sediments in the inner wedge, from Inner Carpathians basement and/or cover. For the middle nappes (Dukla,

Krosno and Skyba), sources are mixed, from north-eastern areas such as the Trans-European Suture Zone or the East

European Margin , and from the intra-basinal highs in the paleo Krosno basins (Kováč, 2016). Mixed sediment may have

545 arrived from the Polish Carpathians along strike (Oszczypko, 2006).

Through the construction of burial diagrams coupled with thermal-history models, we discriminate between sedimentary and

tectonic burial for each nappe. The Magura and Marmarosh nappes stopped their sedimentary burial earlier and accumulated

sediment until the Eocene. Their accretion and deformation lasted, respectively, from 34 to 30 Ma and from 34 to 20 Ma.

The Burkut and Dukla nappes record sedimentation until the Oligocene, while on the Krosno and Skyba nappes

550 sedimentation continued into the early Miocene. The Burkut and Dukla nappes started their accretion as the inner nappes

began their exhumation, around 28-20 Ma (Fig. 13). For the Burkut nappe, exhumation started at 20-18 Ma and corresponds

to the onset of tectonic burial of the Krosno and Skyba nappes. However, the Krosno nappe and the northwest part of the

Skyba nappe started exhuming shortly after 18 Ma, in contrast to the southeast part of the Skyba nappe that was exhumed

around 12 Ma. The more internal Dukla nappe was exhumed at the same time, probably as a result of out-of-sequence

555 thrusting. Early exhumation in the inner wedge from 34 Ma was slow, with a rate of ~0.1 km/My. Following accretion at 28-

18 Ma, exhumation occurred at an increasing rate for every progressive nappe (0.2-0.4 km/My). Final exhumation of the

external nappes after 12 Ma was also rapid, with rates around 0.3 km/My. According to these rates and area estimates from

balanced cross sections, eroded sediments from the Ukrainian Carpathian wedge have been mainly transported into the

Carpathian foreland basin, with little inter-nappe sediment recycling.

560 Given the context of a retreating subduction zone and slab roll-back, the construction of the Ukrainian Carpathians can be

seen as the construction of an accretionary wedge in the Oligocene to the onset of collision in the late Miocene (Fig. 13).

Low-temperature thermochronology pattern of reset/partially reset ages across the wedge may indicate immature wedge

dynamics, as resetting of the thermochronological systems toward the internal part of the wedge should occur if steady-state

is maintained sufficiently long (Willet and Brandon, 2002) during wedge accretion. The inner nappes were accreted against

565   the basement rocks of the active margin, which functioned as the backstop of the wedge. As convergence continued, the wedge grew toward the middle of the basin and accumulation of thrust sheets (Burkut and Dukla nappes) created an (emerged?) orogenic wedge. Downward pull of the slab (more than the orogenic load) created accommodation space toward the foreland. The frontal thrust propagated over an intra-basinal high allowing accretion of the Krosno and Skyba nappes. The deformation and accretion of the outer nappes started as the above-mentioned basement high collided with the

570   subduction zone (continental collision). A last step brought the orogenic wedge onto the passive margin, thrusting the entire wedge onto the outer nappes and the European Platform, synchronous with slab detachment. The foreland was deformed by this last shortening episode and thrusts stopped their propagation at 11.5 Ma in this region (Nemčok et al., 2006).

Data availability

All raw data analysis can be provided by the corresponding author upon request

575   ## Authors contribution

AdL, acquired funding for the project; AdL, and MR, planned the campaign and sampled; ESR, MR, and JG, performed the measurement; ESR, MB and PvdB analyzed the data; MR modelled the data and wrote the manuscript draft; AdL, PvdB, LH, ESR and MB reviewed and edit the manuscript.

Acknowledgements

580   This work is supported by the French National Research Agency in the framework of the "Investissements d'avenir" program (ANR-15-IDEX-02) and is part of the IDEX QUANTIFLUX project. We want to thank Anton Matoshko for his help during the sampling campaign. We thank Francis Coeur, Francois Senebier and Melanie Balvay of the GTC platform at ISTerre for their help with sample processing, mineral separation and fission-track thermochronology.

References

585   Andreucci, B., Castelluccio, A., Jankowski, L., Mazzoli, S., Szaniawski, R., Zattin, M.: Burial and exhumation history of the Polish outer Carpathians: discriminating the role of thrusting and post-thrusting extension. Tectonophysics 608, 866–883, http://dx.doi.org/10.1016/j.tecto.2013.07.030, 2013.

Andreucci, B., Castelluccio, A., Corrado, S., Jankowski, L., Mazzoli, S., Szaniawski, R., and Zattin, M.: Interplay between the thermal evolution of an orogenic wedge and its retro-wedge basin: An example from the Ukrainian Carpathians, Geol.

590   Soc. Am. Bull., 127, 410–427, https://doi.org/10.1130/B31067.1, 2015.

Andreyeva-Grigorovich, A.S., Oszczypko, N., Ślączka, A., Oszczypko-Clowes, M., Savitskaya, N.A., Trofimovicz, N.: New data on the stratigraphy of the folded Miocene zone at the front of the Ukrainian outer Carpathians. Acta Geol. Pol. 58, 325–353, 2008.

595 Ault, A. K., Gautheron, C., and King, G. E.: Innovations in (U–Th)/He, fission track, and trapped charge thermochronometry with applications to earthquakes, weathering, surface-mantle connections, and the growth and decay of mountains, Tectonics, 38, 3705–3739, https://doi.org/10.1029/2018TC005312, 2019.

Barr, T. D. and Dahlen, F. A.: Constraints on friction and stress in the Taiwan fold-and-thrust belt from heat flow and geochronology, Geology, 18, 111–115, doi:10.1130/0091-7613(1990)018<0111:cofasi>2.3.co;2, 1990.

Batt, G. E., Brandon, M. T., Farley, K. A., and Tice, M. R.: Tectonic synthesis of the Olympic Mountains segment of the
600 Cascadia wedge, using two-dimensional thermal and kinematic modeling of thermochronological ages, J. Geophys. Res. 106, 26731–26746, https://doi.org/10.1029/2001jb000288, 2001.

Beyssac, O., Simoes, M., Avouac, J.-P., Farley, K. A., Chen, Y.-G., Chan, Y.-C., and Goffé, B.: Late Cenozoic metamorphic evolution and exhumation of Taiwan, Tectonics, 26, TC6001, https://doi.org/10.1029/2006tc002064, 2007.

Brandon, M. T., Roden-Tice, M. K., and Garver, J. I.: Late Cenozoic exhumation of the Cascadia accretionary wedge in the
605 Olympic Mountains, northwest Washington State, Geol. Soc. Am. Bull., 110, 985–1009, https://doi.org/10.1130/0016-7606(1998)110<0985:lceotc>2.3.co;2, 1998.

Braun, J., van der Beek, P., and Batt, G. E.: Quantitative Thermochronology: Numerical methods for the interpretation of thermochronological data, Cambridge University Press, 271 pp., 2006.

Carlson, W. D., Donelick, R. A., and Ketcham, R. A.: Variability of apatite fission-track annealing kinetics: I. Experimental
610 results, Am. Mineral., 84, 1213–1223, 1999.

Castelluccio, A., Mazzoli, S., Andreucci, B., Jankowski, L., Szaniawski, R., and Zattin, M.: Building and exhumation of the Western Carpathians: New constraints from sequentially restored, balanced cross sections integrated with low-temperature thermochronometry, Tectonics, 35, 2698–2733, https://doi.org/10.1002/2016TC004190, 2016.

Cloetingh, S. A. P. L., Burov, E., Matenco, L., Toussaint, G., Bertotti, G., Andriessen, P. A. M., Wortel, M. J. R., and
615 Spakman, W.: Thermo-mechanical controls on the mode of continental collision in the SE Carpathians (Romania), Earth and Planetary Science Letters, 218, 57–76, https://doi.org/10.1016/S0012-821X(03)00645-9, 2004.

Docin, G.D.: State geological map of Ukraine (M34-30) scale 1: 200 000, State geological research institute UkrSGRI, 1963

Erlanger, E. D., Fellin, M. G., and Willett, S. D.: Exhumation and erosion of the Northern Apennines, Italy: new insights from low-temperature thermochronometers, Solid Earth, 13, 347–365, https://doi.org/10.5194/se-13-347-2022, 2022.

620 Farley, K. A., Wolf, R. A., and Silver, L. T.: The effects of long alpha-stopping distances on (U-Th)/He ages, Geochimica et Cosmochimica Acta, 60, 4223–4229, https://doi.org/10.1016/S0016-7037(96)00193-7, 1996.

Fillon, C., Gautheron, C., and van der Beek, P.: Oligocene–Miocene burial and exhumation of the Southern Pyrenean foreland quantified by low-temperature thermochronology, J. Geol. Soc. London, 170, 67–77, https://doi.org/10.1144/jgs2012-051, 2013.

625 Gągała, Ł., Vergés, J., Saura, E., Malata, T., Ringenbach, J.-C., Werner, P., and Krzywiec, P.: Architecture and orogenic evolution of the northeastern Outer Carpathians from cross-section balancing and forward modeling, Tectonophysics, 532–535, 223–241, https://doi.org/10.1016/j.tecto.2012.02.014, 2012.

Gallagher, K.: Transdimensional inverse thermal history modeling for quantitative thermochronology, J. Geophys. Res., 117, B02408, https://doi.org/10.1029/2011JB008825, 2012.

630 Galetto, A. V., Georgieva, V., Garcia, V. H., Zattin, M., Sobel, E. R., Glodny, J., Bordese, S., Arzadun, G., Bechis, F., Caseli, A. T., Becchio, R.: Cretaceous and Eocene rapid cooling phases in the Southern Andes (36°- 37°S): Insights from low-temperature thermochronology, U-Pb geochronology, and inverse thermal modeling from Domuyo area, Argentina., Tectonics, 40, https://doi.org/10.1029/2020TC006415, 2021.

Gautheron, C., Tassan-Got, L., Barbarand, J., and Pagel, M.: Effect of alpha-damage annealing on apatite (U–Th)/He
635 thermochronology, Chem. Geol., 266, 157–170, https://doi.org/10.1016/j.chemgeo.2009.06.001, 2009.

Gerasimov L.S., Makarov B.O., Chayi S.V., Gerasinova I.I.: State geological map of Ukraine (M34-24) scale 1: 200 000, State geological research institute UkrSGRI, 2005.

Guenthner, W. R., Reiners, P. W., Ketcham, R. A., Nasdala, L., and Giester, G.: Helium diffusion in natural zircon: Radiation damage, anisotropy, and the interpretation of zircon (U-Th)/He thermochronology, Am. J. Sci., 313, 145–198,
640 https://doi.org/10.2475/03.2013.01, 2013.

Handy, M. R., Ustaszewski, K. and Kissling, E.: Reconstructing the Alps–Carpathians–Dinarides as a key to understanding switches in subduction polarity, slab gaps and surface motion, Int J Earth Sci, 104(1), 1–26, doi:10.1007/s00531-014-1060-3, 2015.

Horváth, F. and Cloetingh, S.: Stress-induced late-stage subsidence anomalies in the Pannonian basin, Tectonophysics, 266,
645   287–300, https://doi.org/10.1016/S0040-1951(96)00194-1, 1996.

Hoth, S., Hoffmann-Rothe, A., and Kukowski, N.: Frontal accretion: An internal clock for bivergent wedge deformation and
surface uplift, J. Geophys. Res., 112, B06408, https://doi.org/10.1029/2006JB004357, 2007.

Hurford, A.J., and Green, P.F.: A users' guide to fission track dating calibration, Earth Planet. Sci. Lett., 59, 343-354, 1982.

Husson, L. and Moretti, I.: Thermal regime of fold and thrust belts—an application to the Bolivian sub Andean zone,
650   Tectonophysics, 345, 253–280, https://doi.org/10.1016/s0040-1951(01)00216-5, 2002.

Ketcham, R. A., Carter, A., Donelick, R. A., Barbarand, J., and Hurford, A. J.: Improved modeling of fission-track annealing
in apatite, Am. Mineral., 92, 799–810, https://doi.org/10.2138/am.2007.2281, 2007.

Ketcham, R. A., Gautheron, C., and Tassan-Got, L.: Accounting for long alpha-particle stopping distances in (U–Th–Sm)/He
geochronology: Refinement of the baseline case, Geochimica et Cosmochimica Acta, 75, 7779–7791,
655   https://doi.org/10.1016/j.gca.2011.10.011, 2011.

Konstantinovskaia, E. and Malavieille, J.: Erosion and exhumation in accretionary orogens: Experimental and geological
approaches, Geochem. Geophys. Geosyst., 6, https://doi.org/10.1029/2004GC000794, 2005.

Kotarba, M.J., and Koltun, Y.V.: The origin and habitat of hydrocarbons of the Polish and Ukrainian parts of the Carpathian
Province, in Golonka, J., and Picha, F.J., eds., The Carpathians and Their Foreland: Geology and Hydrocarbon Resources.
660   AAPG Memoir 84, p. 395–442, 2006.Kováč, M.: Paleogene palaeogeography and basin evolution of the Western
Carpathians, Northern Pannonian domain and adjoining areas, 19, 2016.

Kováč, M.: Paleogene palaeogeography and basin evolution of the Western Carpathians, Northern Pannonian domain and
adjoining areas, 19, 2016.

Kovács, I.: Seismic anisotropy and deformation patterns in upper mantle xenoliths from the central Carpathian–Pannonian
665   region: Asthenospheric flow as a driving force for Cenozoic extension and extrusion?, 12, 2012.

Krijgsman, W., and Piller, W.E.: Central and eastern Paratethys regional stages, in Gradstein, F.M., et al., eds., The Geologic
Time Scale 2012: Amsterdam, Elsevier, p. 935–937, 2012.

Matenco, L., Krézsek, C., Merten, S., Schmid, S., Cloetingh, S., and Andriessen, P.: Characteristics of collisional orogens
670   with low topographic build-up: an example from the Carpathians, 22, 155–165, https://doi.org/10.1111/j.1365-
3121.2010.00931.x, 2010.

Matskiv B.V., Pukach B.D., Kovalof Y.V., Vorobkanich V.M.: State geological map of Ukraine (M34-29, M34-35, L34-5) scale 1: 200 000, State geological research institute UkrSGRI, 2008.

675 Matskiv B.V., Pukach B.D., Vorobkaniv V.M., Pastukhanoa S.V., Gnilko O.M.: State geological map of Ukraine (M34-36, M35-31, L34-6, L35-1) scale 1: 200 000, State geological research institute UkrSGRI, 2009.

Mazzoli, S., Jankowski, L., Szaniawski, R., and Zattin, M.: Low-T thermochronometric evidence for post-thrusting (<11 Ma) exhumation in the Western Outer Carpathians, Poland, Comptes Rendus Geoscience, 342, 162–169, https://doi.org/10.1016/j.crte.2009.11.001, 2010.

Merten, S., Matenco, L., Foeken, J. P. T., Stuart, F. M., and Andriessen, P. A. M.: From nappe stacking to out-of-sequence
680 postcollisional deformations: Cretaceous to Quaternary exhumation history of the SE Carpathians assessed by low-temperature thermochronology, Tectonics, 29, https://doi.org/10.1029/2009TC002550, 2010.

Nakapelyukh, M., Bubniak, I., Yegorova, T., Murovskaya, A., Gintov, O., Shlapinskyi, V., and Vikhot, Y.: Balanced geological cross-section of the outer Ukrainian Carpathians along the pancake profile, Journal of Geodynamics, 108, 13–25, https://doi.org/10.1016/j.jog.2017.05.005, 2017.

685 Nakapelyukh, M., Bubniak, I., Bubniak, A., Jonckheere, R., and Ratschbacher, L.: Cenozoic structural evolution, thermal history, and erosion of the Ukrainian Carpathians fold-thrust belt, Tectonophysics, 722, 197–209, https://doi.org/10.1016/j.tecto.2017.11.009, 2018.

Naylor, M. and Sinclair, H. D.: Pro- vs. retro-foreland basins, Basin Res., 20, 285–303, https://doi.org/10.1111/j.1365-2117.2008.00366.x, 2008.

690 Nemcok, M., Pospisil, L., Lexa, J., and Donelick, R. A.: Tertiary subduction and slab break-off model of the Carpathian–Pannonian region, Tectonophysics, 295, 307–340, https://doi.org/10.1016/S0040-1951(98)00092-4, 1998.

Nemčok, M., Pogácsás, G., and Pospíšil, L.: Activity Timing of the Main Tectonic Systems in the Carpathian–Pannonian Region in Relation to the Rollback Destruction of the Lithosphere, in: The Carpathians and Their Foreland: Geology and Hydrocarbon Researces: AAPG Memoir 84, edited by: Golonka, J. and Picha, F. J., The American Association of Petroleum
695 Geologists, Tulsa, Oklahoma, U.S.A., 743–766, https://doi.org/10.1306/985627M843083, 2006.

Oszczypko, N.: Late Jurassic-Miocene evolution of the Outer Carpathian fold-and-thrust belt and its foredeep basin (Western Carpathians, Poland), 25, 2006.

Oszczypko, N., Oszczypko-Clowes, M., Golonka, J., and Krobicki, M.: Position of the Marmarosh Flysch (Eastern Carpathians) and its relation to the Magura Nappe (Western Carpathians), Acta Geologica Hungarica, 48, 259–282,
700 https://doi.org/10.1556/AGeol.48.2005.3.2, 2005.

Pharaoh, T. C.: Palaeozoic terranes and their lithospheric boundaries within the Trans-European Suture Zone (TESZ): a review, Tectonophysics, 314, 17–41, https://doi.org/10.1016/S0040-1951(99)00235-8, 1999.

Popadyuk I., Vul M., Ladyzhensky G., and Shpak P.: Petroleum geology of the Boryslav – Pokuttya zone, the Ukrainian Carpathians, in Golonka J. and Picha F. J., eds., The Carpathians and their foreland: Geology and hydrocarbon resources:
705 AAPG Memoir 84, p. 455 – 466, https://doi.org/10.1306/985732M843075 , 2006.

Roure, F., Roca, E., and Sassi, W.: The Neogene evolution of the outer Carpathian flysch units (Poland, Ukraine and Romania): kinematics of a foreland/fold-and-thrust belt system, Sedimentary Geology, 86, 177–201, https://doi.org/10.1016/0037-0738(93)90139-V, 1993.

710 Royden, L.H.: The tectonic expression slab pull at continental convergent boundaries, Tectonics, 12, 303–325, https://doi.org/10.1029/92tc02248, 1993.

Royden, L. and Karner, G. D.: Flexure of lithosphere beneath Apennine and Carpathian foredeep basins: Evidence for an insufficient topographic load, Am Assoc. Petrol. Geol. Bull, 68, 704–712, https://doi.org/10.1306/ad461372-16f7-11d7-8645000102c1865d, 1984.

715 Royden, L. and Faccenna, C.: Subduction orogeny and the late Cenozoic evolution of the Mediterranean arcs, Ann. Rev. Earth Planet. Sci., 46, 1–29, https://doi.org/10.1146/annurev-earth-060115-012419, 2015.

Seghedi, I., Downes, H., Pécskay, Z., Thirlwall, M. F., Szakács, A., Prychodko, M., and Mattey, D.: Magmagenesis in a subduction-related post-collisional volcanic arc segment: the Ukrainian Carpathians, Lithos, 57, 237–262, https://doi.org/10.1016/S0024-4937(01)00042-1, 2001.

720 Şengül-Uluocak, E., Pysklywec, R. N., Göğüş, O. H., and Ulugergerli, E. U.: Multidimensional Geodynamic Modeling in the Southeast Carpathians: Upper Mantle Flow-Induced Surface Topography Anomalies, Geochem. Geophys. Geosyst., 2019GC008277, https://doi.org/10.1029/2019GC008277, 2019.

Shlapinskyi, V.: Geological map of the Ukrainian Carpathians, scale 1: 100 000. Transcarpathian, Ivano–Frankivsk, Lviv, Tscernivtsi regions. In: Krupsky, Yu.Z. (Ed.), Zvit ZAO "Koncern Nadra", Kyiv, 228 p. (in Ukrainian), 2007.

725

Shlapinskyi, V.: The Geological Architecture of the Skyba, Krosno, DuklyaChornogora Nappes of the Ukrainian Carpathians and Prospects of Oil and Gas (unpublished doctoral thesis). Institute of Geology and Geochemistry of Combustible Minerals, Lviv (in Ukrainian), 2015.

Simpson, G. D. H.: Modelling interactions between fold-thrust belt deformation, foreland flexure and surface mass transport, Basin Research, 18, 125–143, https://doi.org/10.1111/j.1365-2117.2006.00287.x, 2006.

Sinclair, H.: Thrust Wedge/Foreland Basin Systems, in: Tectonics of Sedimentary Basins, edited by: Busby, C. and Azor, A., John Wiley & Sons, Ltd, Chichester, UK, 522–537, https://doi.org/10.1002/9781444347166.ch26, 2012.

Sinclair, H. D., and Naylor, M.: Foreland basin subsidence driven by topographic growth versus plate subduction, Geol. Soc. Am. Bull., 124, 368–379, https://doi.org/10.1130/B30383.1, 2012.

Sperner, B., Ratschbacher, L., and Nemčok, M.: Interplay between subduction retreat and lateral extrusion: Tectonics of the Western Carpathians. Tectonics, v. 21, 1051, doi:10.1029/2001TC901028, 2002.

Stockmal, G. S., Beaumont, C., and Boutilier, R.: Geodynamic models of convergent margin tectonics: Transition from rifted margin to overthrust belt and consequences for foreland-basin development, Am. Assoc. Petrol. Geol. Bull., 70, 181–190, https://doi.org/10.1306/94885656-1704-11d7-8645000102c1865d, 1986.

Ter Voorde, M., de Bruijne, C. H., Cloetingh, S. A. P. L., and Andriessen, P. A. M.: Thermal consequences of thrust faulting: simultaneous versus successive fault activation and exhumation, Earth Planet. Sci. Lett., 223, 395–413, https://doi.org/10.1016/j.epsl.2004.04.026, 2004.

Tiliță, M., Lenkey, L., Mațenco, L., Horváth, F., Surányi, G., and Cloetingh, S.: Heat flow modelling in the Transylvanian basin: Implications for the evolution of the intra-Carpathians area, Global and Planetary Change, 171, 148–166, https://doi.org/10.1016/j.gloplacha.2018.07.007, 2018.

Thomson, S. N., Brandon, M. T., Reiners, P. W., Zattin, M., Isaacson, P. J., and Balestrieri, M. L.: Thermochronologic evidence for orogen-parallel variability in wedge kinematics during extending convergent orogenesis of the northern Apennines, Italy, Geol. Soc. Am. Bull., 122, 1160–1179, https://doi.org/10.1130/b26573.1, 2010.

Van der Beek, P., Robert, X., Mugnier, J.-L., Bernet, M., Huyghe, P., and Labrin, E.: Late Miocene – Recent exhumation of the central Himalaya and recycling in the foreland basin assessed by apatite fission-track thermochronology of Siwalik sediments, Nepal, Basin Res., 18, 413–434, https://doi.org/10.1111/j.1365-2117.2006.00305.x, 2006.

Willett, S. D. and Brandon, M. T.: On steady states in mountain belts, Geology, 30, 175–178, https://doi.org/10.1130/0091-7613(2002)030<0175:ossimb>2.0.co;2, 2002.

Winkler, W. and Slaczka, A.: Sediment dispersal and provenance in the Silesian, Dukla and Magura flysch nappes (Outer
755   Carpathians, Poland), Geol Rundsch, 81, 371–382, https://doi.org/10.1007/BF01828604, 1992.

Wortel, M.J.R., and Spakman, W.: Subduction and slab detachment in the Mediterranean-Carpathian region, Science, 290, 1910–1917, https://doi.org/10.1126/science.290.5498.1910, 2000.

Zayats, H.B.: Deep Structure of the Western Region of Ukraine Based on Seismic Surveys and Directions for Oil and Gas Prospecting. Publishing house «Tsentr Evropy», Lviv in Ukrainian, 2013.

760   Zhou, R., Schoenbohm, L. M., Sobel, E. R., Davis, D. W., and Glodny J.: New constraints on orogenic models of the
southern Central Andean Plateau: Cenozoic basin evolution and bedrock exhumation, Geological Society of America Bulletin, 129, 152-170, 2017.

765

Sample	latitude °N	longitude °E	elevation m	Lithology	Tetonic unit	Stratigraphic age Ma	Thermochronometers
CAR19-045	47.9417	25.14956	731	coarse sandstone	Skyba	Lutetian-Bartonian (47.8-37.8)	AFT, AHe, ZHe
CAR19-047	48.3108	25.07353	366	greenish sandstone	Boryslav-Pokuttia	Ypresian (56-47.8)	AHe, ZHe
CAR19-056	48.806	23.79279	626	grey sandstone	Skyba	Upper-Cretaceous (96-66)	AFT, AHe, ZHe
CAR19-061	48.29	23.38376	223	fine, light grey sandstone	Marmarosh	Bartonian-Priabonian (41.2-33.9)	AFT, AHe, ZHe
CAR19-062	48.4893	23.27509	293	fine, light grey sandstone	Burkut	Cenomanian-Turonian (100.5-89.9)	AFT, AHe, ZHe
CAR19-063	48.5132	23.31984	455	grey sandstone	Burkut	Danian-Ypresian (65.8-47.8)	AFT, AHe, ZHe
CAR19-066	48.8085	22.44757	248	white sandstone	Magura	Lutetian-Bartonian (47.8-37.8)	AFT, AHe, ZHe
CAR19-068	48.957	22.61442	296	yellowish sandstone	Dukla	Campanian-Maastrichtian (83.6-66)	AFT, AHe, ZHe
CAR19-069	48.9759	22.8041	460	yellowish sandstone	Krosno	Aquitanian (27.8-23.03)	AFT, AHe, ZHe
CAR19-070	49.1321	23.03773	708	yellow sandstone	Krosno	Eocene (56-33.9)	AFT
CAR19-072	49.3612	23.01119	387	grey sandstone	Skyba	Rupelian (33.9-27.8)	AFT, AHe, ZHe

Table 1: Sample locations and characteristics

770

Sample	grains	ρ_s	N_s	ρ_i	N_i	ρ_d	$P(\chi^2)$	Dispersion	Central age	2 σ	U	TLn	MTL	Std	Dpar	Dpar err
		10^5 cm^{-2}		10^5 cm^{-2}		10^5 cm^{-2}		%	Ma		ppm		μm		μm	
CAR19-045	75	4.23	1371	18.30	5926	10.80	<<1	48	39.4	6.0	25.0	13.0	11.8	2.3	2.0	0.9
CAR19-056	61	5.03	1230	34.50	8450	10.59	<<1	53	20.3	3.6	49.0	10.0	13.1	2.3	1.7	0.7
CAR19-061	81	4.83	1535	15.50	4937	10.49	<<1	39	47.5	6.6	22.0	21.0	10.8	1.7	1.5	0.8
CAR19-062	67	1.90	488	18.70	4796	10.39	<<1	29	15.9	2.4	27.0	-	-	-	1.7	0.9
CAR19-063	67	1.45	350	16.60	3999	10.29	<<1	41	15.0	2.8	24.0	3.0	12.0	4.0	1.4	1.0
CAR19-066	68	6.55	1247	23.80	4528	10.19	<<1	47	41.1	6.6	35.0	10.0	10.2	2.2	1.5	1.0
CAR19-068	81	1.99	607	25.80	7875	10.09	<<1	25	11.1	1.52	38.0	3.0	8.5	1.6	1.5	1.0
CAR19-069	97	2.53	950	24.10	9043	9.98	<<1	62	16.0	2.8	36.0	9.0	10.5	2.8	1.6	0.6
CAR19-070	31	3.53	360	15.70	1605	9.88	<<1	65	28.1	8.2	24.0	1.0	8.5	0.0	1.5	0.6
CAR19-072	61	2.41	532	15.10	3337	9.78	<<1	59	21.7	4.6	23.0	2.0	13.7	1.2	1.5	0.8

Table 2: Apatite fission-track data. ρ_s: spontaneous track density; N_s: number of spontaneous tracks counted in the sample; ρ_i: induced track density; N_i: number of induced tracks counted on the mica-detector; ρ_d: dosimeter track density; $P(\chi^2)$: Chi-square probability that the sample contains a single age population, U: Uranium content; TLn: number of track lengths measured; MTL: Mean track length; Std: standard deviation of track lengths measurement; Dpar: mean Dpar value for the sample; Dp err: mean error on the Dpar measurement.

Sample	grain	U	Th	Sm	eU	He	ESR	Ft	Uncorrected age	2 σ	Ft corrected ages
		ppm	ppm	ppm	ppm	nmol/g	mm		Ma	Ma	Ma
CAR19-045	045-a1	7.6	18.6	16.5	12.0	0.4	69.08	0.78	6.4	0.2	8.2
	045-a2	4.5	36.1	13.1	13.0	0.9	61.57	0.76	12.9	0.5	17.0
	045-a3	10.4	68.2	24.8	26.4	1.1	88.23	0.83	7.6	0.2	9.2
CAR19-047	*047-a1*	*9.4*	*2.1*	*60.8*	*9.9*	*0.0*	76.87	*0.80*	*0.1*	*0.1*	*0.1*
	047-a2	25.3	31.6	17.6	32.7	1.4	88.18	0.83	7.9	0.1	9.5
CAR19-056	056-a1	24.7	78.8	48.6	43.2	1.7	60.46	0.75	7.4	0.2	9.8
	056-a2	44.7	180.3	22.7	87.1	3.4	65.99	0.77	7.1	0.2	9.2
	056-a3	136.8	194.4	60.3	182.5	6.6	59.30	0.75	6.7	0.1	8.9
CAR19-061	061-a1	4.4	28.1	41.0	11.0	0.7	54.91	0.73	10.6	0.8	14.6
	061-a2	6.6	13.6	23.1	9.8	0.6	62.88	0.76	11.3	0.5	14.8
	061-a3	14.6	5.5	9.1	15.9	1.8	60.81	0.75	20.3	0.7	27.0
CAR19-062	062-a1	12.0	44.8	22.1	22.5	4.0	74.63	0.80	32.8	0.6	41.1
	062-a2	11.0	89.0	4.1	31.9	1.4	62.89	0.76	8.2	0.4	10.7
	062-a3	*1.8*	*45.5*	*5.4*	*12.5*	*0.2*	71.08	*0.79*	*2.7*	*0.1*	*3.5*
CAR19-063	063-a1	5.9	18.7	3.8	10.3	0.4	68.43	0.78	7.3	0.3	9.3
CAR19-066	066-a1	44.9	128.4	6.8	75.1	4.2	70.34	0.79	10.2	0.2	13.0
	066-a2	29.2	22.1	21.6	34.4	8.0	67.91	0.78	42.9	0.7	55.0
	066-a3	7.5	41.7	12.3	17.2	0.6	54.01	0.72	6.5	0.5	9.1
CAR19-068	068-a1	16.0	387.7	52.7	107.1	2.9	63.10	0.76	5.0	0.2	6.6
	068-a2	22.4	291.8	39.1	91.0	2.8	67.40	0.78	5.6	0.3	7.2
	068-a3	27.6	345.9	44.9	108.9	3.2	61.67	0.76	5.4	0.1	7.1
CAR19-069	069-a1	34.9	116.2	7.5	62.2	3.2	68.52	0.78	9.5	0.1	12.2
	069-a2	59.7	242.4	26.5	116.7	5.0	80.53	0.72	7.9	0.1	11.0
	069-a3	37.6	82.8	44.5	57.1	3.5	77.18	0.81	11.1	0.2	13.8
CAR19-072	072-a1	7.6	22.9	11.7	13.0	1.0	66.55	0.77	14.2	0.6	18.4
	072-a2	35.0	5.1	21.8	36.2	4.6	72.61	0.79	23.5	0.3	29.6

Table 3: Apatite (U-Th-Sm)/He data. Ages in italics are considered outliers and were not used in the models and for interpretations. eU: equivalent Uranium content; ESR: equivalent spherical radius; 2σ: weighted 2σ analytical uncertainty from analysis of age standards.

Sample	grain	U	Th	Sm	eU	He	ESR	Ft	Uncorrected age	2 σ	Ft corrected ages
		ppm	ppm	ppm	ppm	nmol/g	mm		Ma	Ma	Ma
CAR19-045	*045-z1*	*2.3*	*28.6*	*0.7*	*9.0*	*0.9*	*79.5*	*0.80*	*19.2*	*0.6*	*24.2*
	045-z2	*0.8*	*5.3*	*0.3*	*2.0*	*0.1*	*57.6*	*0.77*	*8.5*	*2.4*	*11.0*
	045-z3	483.7	74.9	0.6	501.4	704.9	83.6	0.85	254.9	2.3	298.5
CAR19-047	047-z1	66.0	62.8	0.4	80.8	164.9	105.4	0.88	367.3	2.6	417.4
	047-z2	54.1	73.8	0.7	71.5	71.4	61.4	0.79	182.6	4.7	229.1
CAR19-056	056-z1	52.3	77.3	0.5	70.5	150.2	55.4	0.77	383.1	15.7	491.7
	056-z2	*2.4*	*70.1*	*2.5*	*18.8*	*1.2*	*70.8*	*0.81*	*11.8*	*0.8*	*14.6*
	056-z3	98.8	123.4	1.0	127.8	259.7	80.9	0.84	365.9	4.8	432.3
	056-z4	41.8	25.5	0.2	47.7	71.8	72.1	0.83	272.8	3.3	328.7
CAR19-061	061-z1	212.4	61.2	0.3	226.8	111.2	60.4	0.80	90.3	0.8	113.2
	061-z2	274.9	132.0	0.6	306.0	121.2	67.0	0.81	73.0	0.9	89.6
	061-z3	345.3	74.8	0.6	362.9	135.8	64.1	0.79	69.0	0.8	87.0
	061-z4	853.2	260.8	1.3	914.4	364.2	61.9	0.80	73.4	0.5	91.6
	061-z5	111.5	43.8	0.6	121.7	63.2	65.6	0.81	95.5	1.2	117.6
CAR19-062	062-z1	47.0	35.7	0.3	55.4	31.6	66.8	0.81	104.6	1.4	128.6
	062-z2	204.8	190.1	2.5	249.5	120.6	61.9	0.79	88.9	1.8	112.4

Sample	Grain										
	062-z3	74.6	111.8	0.4	100.8	58.3	72.2	0.82	106.1	1.3	128.7
	062-z5	167.8	55.6	0.5	180.9	87.9	56.6	0.78	89.4	1.5	114.0
	063-z1	39.9	51.4	0.2	52.0	20.9	76.5	0.83	73.8	0.8	89.0
	063-z2	65.1	39.8	0.1	74.5	40.6	68.3	0.81	100.3	1.0	123.5
CAR19-063	063-z3	144.9	55.9	0.2	158.1	95.2	106.2	0.88	110.7	2.2	125.5
	063-z4	534.8	60.5	0.5	549.0	411.5	55.1	0.78	137.4	1.6	175.9
	063-z5	372.9	197.6	3.1	419.3	165.8	39.1	0.69	72.8	1.2	105.1
	066-z1	211.9	35.0	0.7	220.1	98.5	64.4	0.81	82.4	1.3	101.8
	066-z2	115.1	184.1	1.1	158.4	86.4	83.3	0.84	100.2	1.7	118.9
CAR19-066	066-z3	125.5	140.1	1.5	158.4	190.9	44.8	0.72	219.4	3.7	300.7
	066-z4	272.4	34.4	0.5	280.5	85.3	56.7	0.78	56.2	0.7	71.6
	066-z5	24.6	23.1	0.3	30.0	12.5	67.6	0.81	76.4	1.3	94.6
	068-z1	227.7	135.7	0.6	259.6	307.2	65.5	0.81	215.4	2.4	265.1
CAR19-068	068-z2	737.8	141.3	1.2	771.0	522.2	66.8	0.81	124.3	1.6	152.2
	068-z3	132.6	26.8	0.2	138.9	146.8	72.7	0.83	192.7	1.8	231.6
	069-z1	106.0	12.6	0.1	109.0	99.3	59.3	0.79	166.6	2.2	209.2
	069-z2	124.5	67.4	0.3	140.3	58.5	57.8	0.79	76.9	1.5	97.7
CAR19-069	069-z3	124.3	93.5	0.8	146.3	39.9	60.7	0.79	50.4	0.6	63.4
	069-z4	126.2	87.3	0.3	146.7	68.4	62.3	0.80	85.9	1.4	107.2
	069-z5	*0.7*	*8.6*	*2.9*	*2.7*	*0.5*	*66.0*	*0.80*	*34.5*	*1.8*	*43.4*
	072-z1	405.6	120.0	0.6	433.8	185.5	58.6	0.79	78.8	0.8	99.6
CAR19-072	*072-z2*	*0.5*	*3.4*	*2.1*	*1.3*	*0.8*	*60.1*	*0.78*	*105.5*	*4.0*	*135.0*
	072-z3	495.9	266.7	3.4	558.5	516.8	62.6	0.80	169.1	2.4	210.3

Table 4: Zircon (U-Th-Sm)/He data. Ages in italics are considered outliers and were not used in the models and for interpretations. eU: equivalent Uranium content; ESR: equivalent spherical radius; 2σ: weighted 2σ analytical uncertainty from analysis of age standards